AGU PUBLICATIONS

Geophysical Research Letters

RESEARCH LETTER
10.1002/2016GL072335

Key Points:
- The Franklin large igneous province was coincident with onset of the Sturtian Snowball Earth glaciation
- Multiyear to decadal fissure eruptions can inject enough sulfur aerosols to the stratosphere to initiate Snowball Earth
- Cold background climate states are sensitive to ice-albedo catastrophe because tropopause height is a function of surface temperature

Supporting Information:
- Supporting Information S1

Correspondence to:
F. A. Macdonald,
fmacdon@eps.harvard.edu

Citation:
Macdonald, F. A., and R. Wordsworth (2017), Initiation of Snowball Earth with volcanic sulfur aerosol emissions, *Geophys. Res. Lett.*, *44*, doi:10.1002/2016GL072335.

Received 12 DEC 2016
Accepted 7 FEB 2017
Accepted article online 8 FEB 2017

Initiation of Snowball Earth with volcanic sulfur aerosol emissions

F. A. Macdonald[1] and **R. Wordsworth**[1,2]

[1]Department of Earth and Planetary Sciences, Harvard University, Cambridge, Massachusetts, USA, [2]School of Engineering and Applied Sciences, Harvard University, Cambridge, Massachusetts, USA

Abstract We propose that the first Neoproterozoic Snowball Earth event, the Sturtian glaciation, was initiated by the injection of sulfate aerosols into the stratosphere. Geochronological data indicate that the Natkusiak magmatic assemblage of the Franklin large igneous province coincided with onset of the Sturtian glaciation. The Natkusiak was emplaced into an evaporite basin and entrained significant quantities of sulfur, which would have led to extensive SO_2 and H_2S outgassing in hot convective plumes. The largest of these plumes could have penetrated the tropopause, leading to stratospheric sulfate aerosol formation and an albedo increase sufficient to force a Snowball. Radiative forcing was maximized by the equatorial location of the Franklin and the cool Neoproterozoic background climate, which would have lowered the tropopause height, increasing the rate of stratospheric aerosol injection. Our results have implications for understanding Phanerozoic mass extinction events, exoplanet habitability, and aerosol perturbations to the present-day climate.

1. Introduction

The Neoproterozoic Era witnessed two Snowball Earth glaciations, the ~717–660 Ma Sturtian glaciation and the ~645–635 Ma Marinoan glaciation [*Rooney et al.*, 2015]. These glaciations are the largest episodes of climate change in the geological record [*Hoffman and Schrag*, 2002], yet we do not understand how they were initiated. Of particular importance is the transition into the first Neoproterozoic Snowball event, the Sturtian glaciation (Figure 1), which was preceded by over one billion years of apparently clement conditions.

Previously, it has been proposed that the Neoproterozoic climate was cool as a result of the predominance of equatorial continents with newly rifted margins and increased planetary weatherability [*Cox et al.*, 2016; *Godderis et al.*, 2003; *Macdonald et al.*, 2010; *Rooney et al.*, 2014; *Schrag et al.*, 2002]. The rifting of the supercontinent Rodinia occurred near the equator from ~850 to 650 Ma [*Li et al.*, 2013] and was accompanied by the emplacement of multiple large igneous provinces (LIPs), including the Franklin LIP (Figure 1a). These newly rifted margins and the emplacement of rift-related LIPs at low latitude would have increased global weatherability [*Godderis et al.*, 2003; *Macdonald et al.*, 2010; *Rooney et al.*, 2014] and phosphorous input to the oceans, which would have led to more organic carbon productivity and burial in tropical deltas [*Cox et al.*, 2016]. A low-latitude paleogeography may have also limited the "land area feedback" in which silicate weathering rates decline with the growth of ice sheets on high-latitude continents [*Schrag et al.*, 2002]. Hence, Neoproterozoic paleogeography may have been more sensitive to ice-albedo runaway. Alternatively, it has been proposed that long-term Neoproterozoic cooling was due to decreased volcanic outgassing [*McKenzie et al.*, 2016]. Whether it was a change in geological sources or sinks of CO_2, or a change in the sensitivity of the silicate weathering feedback (in the sense of *Maher and Chamberlain* [2014]), the fact that there were two Neoproterozoic Snowball Earth events in rapid succession suggests that background conditions played an important role.

From this cool background climate state, various proximal triggers for the Snowball transition have also been proposed to overcome the silicate weathering feedback, including short-term perturbations to the greenhouse gas inventory [*Schrag et al.*, 2002; *Tziperman et al.*, 2011] and/or the planetary albedo [*Bendtsen and Bjerrum*, 2002; *Feulner et al.*, 2015; *Stern et al.*, 2008]. Previous explanations invoking a short-term drawdown of CO_2 or methane were motivated by an apparent correlation between perturbations to the carbon cycle and the onset of glaciation [*Schrag et al.*, 2002; *Tziperman et al.*, 2011]. However, recent geochronology has demonstrated that the pre-Sturtian Islay carbon isotope excursion occurred more than 10 Myr before the initiation of the Sturtian by 716.5 ± 0.2 Ma [*Macdonald et al.*, 2010; *Rooney et al.*, 2014; *Strauss et al.*, 2014], ruling out a direct link. Albedo changes due to the emergence of eukaryotic algae [*Feulner et al.*, 2015] rely on the coincidence of a putative evolutionary milestone for which there is no evidence. Finally, others

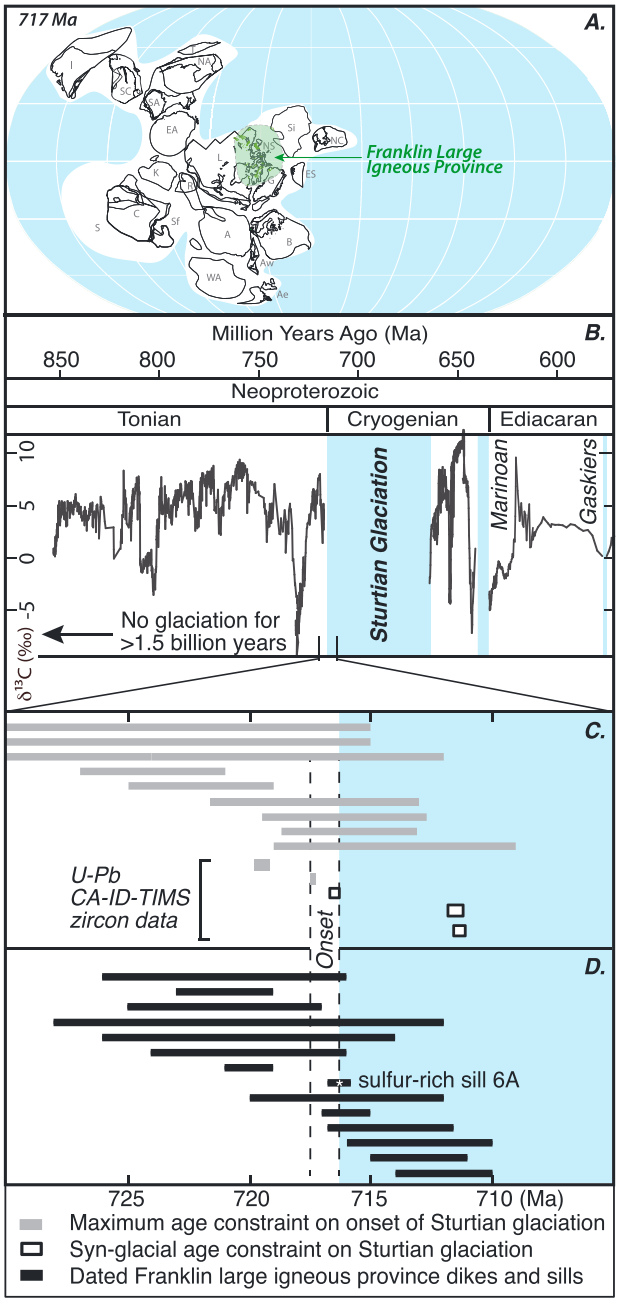

Figure 1. Paleogeographic and geochronological constraints on the onset of the Sturtian glaciation and the Franklin Large Igneous Province. (a) Neoproterozoic paleogeography modified from *Li et al.* [2013] and *Zhang et al.* [2013]). I = India; SA = southern Australia; NA = northern Australia; T = Tarim; SC = South China; M = Mongolia; EA = East Antarctica; Si = Siberia; NC = North China; L = Laurentia; NS = North Slope; ES = East Svalbard; G = Greenland; B = Baltica; A = Amazonia; WA = West Africa; Aw = western Avalonia; Ae = eastern Avalonia; Sf = So Francisco; C = Congo; K = Kalahari; R = Rio Plata. (b) Neoproterozoic timeline with carbon isotope chemostratigraphy, modified from *Cox et al.* [2016]. (c) Geochronological constraints on the onset of the Sturtian glaciation. (d) Geochronological constraints on the Franklin large igneous province. Geochronological data and sources are in Table S1 in the supporting information. Note that the Franklin large igneous province erupted at the equator, and the most precise date of sulfur-rich sills correlate with onset of the Sturtian glaciation, but the carbon isotope excursions do not.

have invoked albedo forcing by meteorite impacts or explosive felsic volcanism [*Bendtsen and Bjerrum*, 2002; *Stern et al.*, 2008]. However, there is no evidence for a major meteorite impact at the time of the Sturtian onset, and albedo perturbations on the timescale of less than a year are unlikely to drive runaway glaciation. Here we propose an alternative scenario, in which multiyear to decadal emissions of sulfur from the Franklin LIP were the proximal trigger that caused the Sturtian Snowball transition.

2. Synchronicity of the Sturtian Snowball Glaciation With Eruption of the Franklin LIP

While the Islay carbon isotope excursion is not synchronous with the Sturtian Snowball glaciation (Figure 1b), the emplacement of the largest Neoproterozoic LIP is. The most precise date on the initiation of the Sturtian glaciation comes from Yukon, Canada, where onset is bracketed between U/Pb zircon dates of 717.4 ± 0.1 and 716.5 ± 0.2 Ma [*Macdonald et al.*, 2010] (Figure 1c). These dates are indistinguishable from the most precise date on the Franklin LIP of 716.3 ± 0.5 Ma [*Macdonald et al.*, 2010] (Figure 1d). Volcanic rocks associated with the Franklin LIP cover an area of >3 Mkm^2 over northern Laurentia and southern Siberia [*Ernst et al.*, 2016] (Figure 1a), which was at equatorial latitudes during its formation [*Denyszyn et al.*, 2009b; *Macdonald et al.*, 2010]. On Victoria Island of the Canadian Arctic, the Franklin LIP is represented by the Natkusiak magmatic assemblage, which consists of basalt and gabbroic dikes and sills that intruded carbonate, organic-rich shale, and sulfur evaporite of the Shaler Supergroup [*Dostal et al.*, 1986]. The amount

of metamorphic CO_2 released from the emplacement of gabbroic sills of the Natkusiak assemblage was small relative to background levels and likely did not have a significant climate effect [*Nabelek et al*., 2014]. However, due to melting and assimilation of sulfur from the evaporites, many of the sills and dikes have extremely high sulfur concentrations, ranging from 100 to 100,000 ppm [*Bedard et al*., 2016], and sulfur isotope compositions indicative of contamination from entrained sedimentary rocks (see Figure S2 in the supporting information). Finally, these sulfur-rich sills are the same sills that have been dated at 716.3 ± 0.5 Ma, which is synchronous within error with the Sturtian glaciation onset [*Macdonald et al*., 2010] (Figure 1c). Inspired by these observations, we propose that the emplacement of the Franklin LIP near the equator into a sulfur-rich basin and subsequent sulfur emission to the atmosphere was the critical event that initiated the Sturtian Snowball Earth.

3. Volcanic Plume, Aerosol, and Climate Modeling

During a volcanic eruption, sulfur is outgassed as a combination of SO_2 and H_2S [*Textor et al*., 2003]. Once in the atmosphere, these gases react with O_2, H_2O, and OH to form H_2SO_4, which condenses with H_2O onto condensation nuclei to form radiatively active sulfate aerosols [*Turco et al*., 1979a]. Weak volcanic plumes inject sulfur into the troposphere, where sulfate aerosols are consumed in days to weeks and have little long-term radiative effect [*Chin et al*., 1996]. Conversely, strong plumes penetrate the tropopause and reach the stratosphere, where H_2SO_4 aerosols can have lifetimes of a year or more [*McCormick et al*., 1995].

Unlike explosive volcanic eruptions such as the 1991 Pinatubo event, the eruptions associated with the Franklin LIP were basaltic in nature, leading to large fire fountains that would have driven hot convective plumes into the atmosphere [*Stothers et al*., 1986]. This has two major consequences. First, the probability of a hot volcanic plume penetrating the tropopause is determined by the degree of thermal energy at the plume base, which can be very high given that basaltic magmas typically have temperatures of 1000 K or more. Second, and most critically, basaltic eruption sequences during LIP formation can occur over very long time periods (years to decades), potentially causing a much longer-term climate impact [*Self et al*., 2014].

To evaluate our hypothesis that the Sturtian glaciation was initiated by the creation of sulfate aerosols from equatorial basaltic volcanism, we modeled the height to which hot, buoyant sulfur-bearing plumes from fire fountains could reach in the atmosphere, the chemical and microphysical evolution of sulfur in the atmosphere, and the radiative effects of sulfate aerosols once they formed. To simulate the volcanic plumes, we used a one-dimensional steady state model incorporating turbulent entrainment. This relatively simple approach is justified based on extensive previous comparisons with observations and laboratory experiments (see discussion in the supporting information). Our sulfur aerosol microphysics model is sectional (82 bins total) and incorporates particle growth, coagulation, sedimentation, and mixing. Sulfate aerosol radiative forcing was calculated using Mie theory and a one-dimensional radiative-convective correlated-*k* model [*Wordsworth et al*., 2010; *Wordsworth et al*., 2013]. We also used this model to provide atmospheric temperature-pressure profiles as input to the volcanic plume model. A complete description of our modeling approach is given in the supporting information.

4. Results

First, we investigated the dependence of the maximum thermal volcanic plume height on the strength of an individual Franklin LIP eruption and on the background climate. Our modeling indicates that plume height is a strong function of volume eruption rate, with eruption rates of 10^4–10^5 m^3/s leading to plume heights greater than the present-day tropical tropopause (~12 km) under Neoproterozoic atmospheric conditions (Figure 2). We estimate these rates to be representative of the peak values produced during eruptions associated with the Franklin LIP (see supporting information). Furthermore, our climate modeling shows that tropopause height is a strong function of surface temperature (Figure 2a). This is because a warmer surface injects more water vapor into the atmosphere, reducing the lapse rate. Hence, very warm climates can "shield" the Earth from stratospheric aerosol injection by even the largest volcanic plumes [see also *Glaze et al*., 2017]. Conversely, a cool background climate in the Neoproterozoic would have made it a particularly dangerous time for a sequence of large basaltic eruptions to occur.

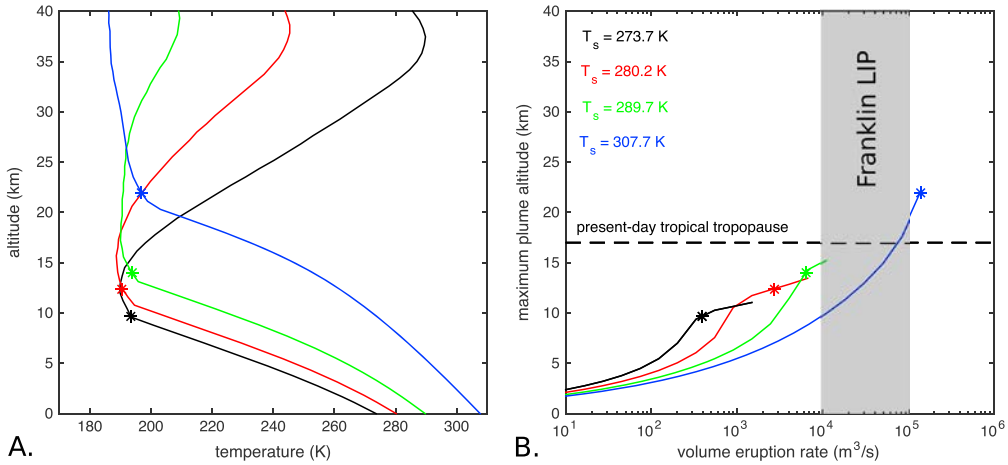

Figure 2. (a) Equilibrium atmospheric temperature profiles produced from the radiative-convective climate model for varying CO_2 concentrations under Neoproterozoic conditions. The black, red, green, and blue lines correspond to simulations where the background CO_2 levels were 30, 300, 3000, and 30,000 ppm, respectively. (b) Maximum Franklin LIP plume height as a function of volume eruption rate. In both panels, asterisks indicate tropopause height, defined as where the lapse rate first drops below 2 K/km. The grey box brackets the maximum plausible volume eruption rate during formation of the Franklin LIP (see the supporting information).

Our microphysical model converts SO_2 and H_2S gas to H_2SO_4 aerosols on a time scale of 30–40 days. Once formed, the aerosols remain in the stratosphere for 1–2 years, with the aerosol loading peaking in the first 3–6 months, in agreement with observations of the 1991 Pinatubo eruption (see the supporting information). We find that the radiative forcing caused by episodic injections of SO_2 into the equatorial stratosphere increases with the quantity of SO_2 injected (Figure 3a), but the increase is sublinear due to particle coagulation, which increases mean particle size and sedimentation rate for large eruptions [*Pinto et al.*, 1989]. For a single eruption, mean global forcing in the following year increases from $-2.7\ W/m^2$ given 20 Mt SO_2 injection (cf. Pinatubo [*McCormick et al.*, 1995]) to $-12\ W/m^2$ for 500 Mt SO_2 (sensitivity to parameters described in the supporting information). Estimating the rate at which sulfur was released from the Franklin LIP on a decadal time scale is challenging, but 500 Mt/yr is similar to estimates of SO_2 release rate from more recent LIPs [*Self et al.*, 2014]. For comparison, the radiative forcing due to CO_2 doubling on the present-day Earth is around $3.7\ W/m^2$ [*Myhre et al.*, 1998].

The eruption sequence of fissure eruptions associated with a LIP is poorly constrained. The best historical analog is the 1783–1784 Laki fissure eruption in Iceland, which emitted ~122 Mt SO_2 over 8 months with ~10 pulses that produced eruptive columns extending 9–13 km [*Thordarson and Self*, 2003]. However, many larger flow fields have been identified in the geological record, which require longer total durations [*Self et al.*, 2014]. If these eruptions had higher magma output rates than Laki, different types of lava would have been produced. For example, using peak output rates from Hawaii and Laki, *Thordarson and Self* [1998] estimated that the 1300 km^3 Roza flow field of the Columbia River Basalt Group formed in ~10–20 years. Larger flows, such as those associated with the Deccan and Siberian Traps, may have lasted an order of magnitude longer [*Self et al.*, 2014] and had multiple eruptive centers. Nonetheless, because a robust eruption time series for a multiyear fissure eruption does not exist, particularly for the sulfur release from an fissure eruption through a sulfur-rich basin, we model the radiative effect of pulsed yearly equatorial volcanic eruptions under Neoproterozoic conditions assuming 20, 100, and 500 Mt of SO_2 injection to the stratosphere (Figure 3a). This covers the range of SO_2 emissions from the historical Pinatubo and Laki eruptions over longer time periods and also explores the larger SO_2 concentrations estimated for the Franklin LIP.

The ability of volcanic aerosols to force a Snowball transition depends on both the starting climate state and on the rate at which the upper layers of the tropical ocean can cool. Based on radiative-convective modeling, we estimate that a $-10\ W/m^2$ global mean aerosol radiative forcing would be sufficient to cause runaway glaciation for CO_2 levels of 3000 ppm (Figure 3b). These CO_2 levels yield approximately present-day global mean temperatures in our model given the fainter Neoproterozoic Sun. For lower background CO_2 levels, as might

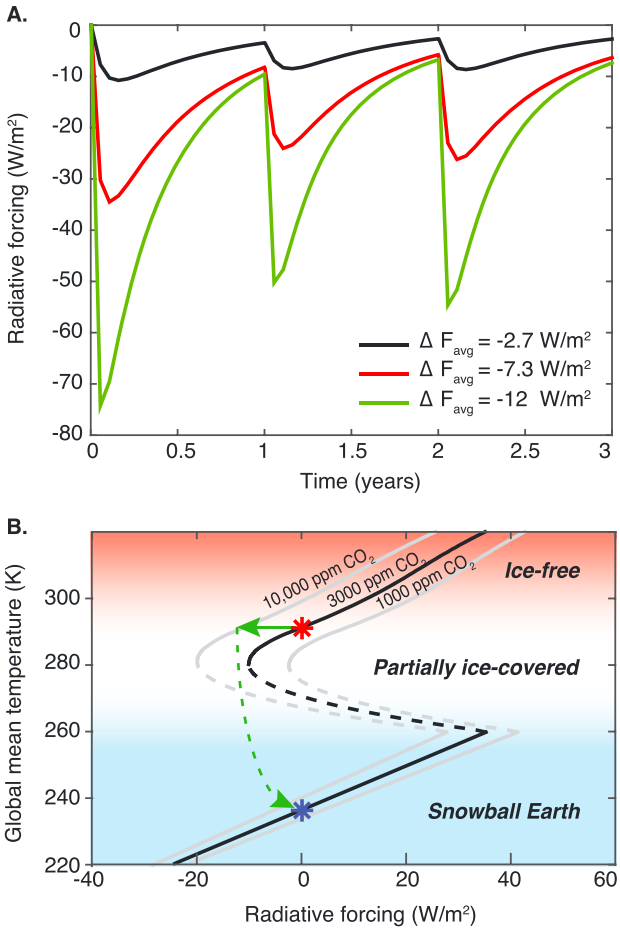

Figure 3. The effect of volcanic sulfate aerosol emission on global climate. (a) Equatorial radiative forcing due to yearly equatorial volcanic eruptions under Neoproterozoic conditions. The black, red, and green lines show simulations assuming 20, 100, and 500 Mt of SO_2 injection to the stratosphere. Annual global mean forcings are also displayed. (b) Bifurcation diagram of global mean temperature versus radiative forcing defined as the difference between outgoing longwave radiation and absorbed solar radiation. The dashed lines are unstable states. Starting from a mean surface temperature close to present day (red star), a negative radiative forcing of $< -10\,W/m^2$ is sufficient to push the Neoproterozoic Earth (green line) into a Snowball state (blue star). Starting from a colder initial state, the required radiative forcing is lower.

be expected in a cool background climate, a Snowball transition could have been caused by a correspondingly lower radiative forcing. A simple calculation assuming an ocean mixing layer depth of 50 m yields a time scale of order 3 years to drive equatorial sea surface temperatures to the freezing point of water and commence a Snowball transition (see the supporting information). Hence, a sequence of large, sulfur-rich eruptions of the type shown in Figure 3a may have been sufficient to drive a runaway ice-albedo event.

Estimates of the Snowball cooling time scale from present-day conditions using general circulation models coupled to a dynamic ocean yield longer time scales (decades to several hundred years, depending on the initial climate state), due to the enhanced vertical ocean mixing driven by surface cooling in those models [*Voigt et al.*, 2011]. Many aspects of mixing in the present-day ocean remain poorly captured by numerical models [*Wunsch and Ferrari*, 2004], so the extrapolation to the Snowball regime is challenging. Nonetheless, if these estimates are robust, they suggest that the climate state before the Franklin LIP erupted would have needed to be colder than that of present-day Earth to allow sulfate aerosol forcing to drive a transition. They also suggest that another reason the 14.98 Ma Roza flow failed to initiate a Snowball was because it erupted during the Miocene climatic optimum, when higher temperatures would have required a significantly longer time scale to freeze the surface ocean.

5. Discussion

If the Franklin LIP caused a Snowball Earth, then why are other LIPs not also associated with Snowball Earth events? The Siberian Traps, which erupted around 250 Ma at the end of the Permian, are similar in size to the Franklin LIP, but instead of cooling, they appear to be associated with warming and extinction [*Ganino and Arndt*, 2009]. Another LIP, the Central Atlantic Magmatic Province (CAMP), may have caused temporary cooling followed by warming [*Schoene et al.*, 2010]. The different outcomes are likely related to several factors: the background climate conditions, changes in background planetary albedo with different paleogeography, the latitude of the eruptions, the composition of the country rock that the LIPs were emplaced into (a sulfate-rich basin, coal deposits, and an ancient mountain belt for the Franklin, Siberian Traps, and CAMP, respectively), and timing of SO_2 injection relative to the cumulative release of gases such as CO_2. Although Neoproterozoic paleogeography likely favored a cool climate [*Li et al.*, 2013; *Marshall et al.*, 1988], the Siberian Traps and CAMP erupted during the ice-free Late Permian and Late Triassic, respectively, when warm conditions

extended to Earth's polar regions [*Taylor et al*., 1992]. Consequently, there would have been a higher tropopause that would have prevented stratospheric aerosol injection by all but the most powerful volcanic eruptions (Figure 2). Moreover, the Siberian Traps erupted at high latitude, whereas the CAMP and Franklin LIP erupted at equatorial latitudes [*Denyszyn et al*., 2009b]. Consequently, albedo changes associated with the Siberian Traps would have primarily affected mid-to-high latitudes in one hemisphere, whereas the CAMP and Franklin LIP would have maximized albedo at low latitude, where solar forcing is highest. Because aerosol radiative forcing is most negative when surface albedo is low, and a high-latitude eruption in a cold climate occurs over snow or sea ice, an equatorial eruption is far more effective at forcing a Snowball transition than a high latitude one (see the supporting information). Deeper in Earth's past, in the Archean and Proterozoic, a warmer climate caused by elevated levels of CO_2 or other greenhouse gases [e.g., *Feulner*, 2012; *Wordsworth and Pierrehumbert*, 2013b] may have elevated the tropopause sufficiently to shield the Earth continuously from significant stratospheric sulfate aerosol injection.

The geological record preserves evidence for two Cryogenian glaciations, the Sturtian and the Marinoan. Although there is not evidence for a LIP during the onset of the Marinoan glaciation, this may be a matter of preservation. The low-latitude rifting of Rodinia continued throughout the Neoproterozoic, and it is likely that this was associated with additional LIPs. Geochronological constraints suggest that the Sturtian glaciation lasted ~58 Myr and that the nonglacial interlude before the Marinoan started was short, between 8.6 and 19.4 Myr [*Rooney et al*., 2014]. If planetary weatherability remained high during the Cryogenian due to continued low-latitude paleogeography and recently emplaced continental flood basalt provinces [*Cox et al*., 2016], transport-limited weathering in the aftermath of the Sturtian glaciation may have returned the Earth on a 10 Myr time scale to a climate state sensitive to further short-term perturbations in the planetary albedo [*Mills et al*., 2011]. After the Marinoan glaciation, the removal of a basaltic carapace and drift of continents to higher latitudes [*Li et al*., 2013] likely reduced global weatherability and climate sensitivity.

6. Conclusion

Based on a combination of geological evidence and atmospheric modeling, we have proposed that the proximal trigger for the Sturtian Snowball Earth was a sudden increase in planetary albedo caused by the emission of sulfate aerosols from basaltic volcanism. Further tests of our hypothesis will be possible via tighter constraints on the geochronology of the Sturtian glaciation and the Franklin LIP, and better estimates of sulfur release with melt inclusion studies along with three-dimensional coupled ocean-atmosphere modeling of the climate effect of stratospheric aerosol emissions. Mercury anomalies have been observed in sedimentary records that span the Permian-Triassic and Triassic-Jurassic boundaries and have been attributed to the Siberian Traps and CAMP, respectively [*Thibodeau and Bergquist*, 2017, and references therein]. Our model predicts that similar mercury signals will be present in sedimentary successions deposited during onset of the Sturtian glaciation.

Our proposed scenario for initiation of the Sturtian has several important implications beyond the Neoproterozoic. In the Phanerozoic, the correlation of LIPs and meteorite impacts with both glaciations and mass extinction events has long suggested a causal link. However, our results imply that the timing and location of major volcanic and impact events may matter as much as, or more than, their overall magnitude. For exoplanets, our results indicate that volcanically active planets may be much more vulnerable to Snowball transitions than traditional habitable zone ideas based on the carbonate-silicate cycle [*Kasting et al*., 1993] would suggest. Finally, if the largest known glaciation event in Earth's history was indeed triggered by stratospheric sulfate aerosols, this should give some caution to similar geo-engineering strategies proposed recently to decrease or eliminate anthropogenic climate change [*Rasch et al*., 2008].

Acknowledgments
The supporting information describes the materials and methods used, and model validation and sensitivity tests; includes four tables and 10 figures, and cites the additional references.

References

Anderson, G. P., S. Clough, F. Kneizys, J. Chetwynd, and E. P. Shettle (1986), AFGL atmospheric constituent profiles (0.120 km), *Rep*., DTIC Document.

Baldwin, G. J., E. C. Turner, and B. S. Kamber (2016), Tectonic controls on distribution and stratigraphy of the Cryogenian Rapitan iron formation, northwestern Canada, *Precambrian Res.*, *278*, 303–322.

Barkstrom, B. R. (1984), The Earth Radiation Budget Experiment (ERBE), *Bull. Am. Meteorol. Soc.*, *65*(11), 1170–1185.

Bedard, J. H., et al. (2012), Falut-mediated melt ascent in a Neoproterozoic continental flood basalt province, the Franklin sills, Victoria Island, Canada, *Geol. Soc. Am. Bull.*, *124*(5/6), 723–736.

Bedard, J. H., et al. (2016), Geochemical database of Franklin sills, Natkusiak Basalts and Shaler Supergroup rocks, Victoria Island, Northwest Territories, and correlatives from Nunavut and the mainland, *Geol. Surv. Canada Open File*, *8009*, 1.
Bendtsen, J., and C. J. Bjerrum (2002), Vulnerability of climate of Earth to sudden changes in insolation, *Geophys. Res. Lett.*, *29*(15), 1706, doi:10.1029/2002GL014829.
Black, B. A., L. T. Elkins-Tanton, M. C. Rowe, and I. U. Peate (2012), Magnitude and consequences of volatile release from the Siberian Traps, *Earth Planet. Sci. Lett.*, *317*, 363–373.
Bowring, S. A., J. P. Grotzinger, D. J. Condon, J. Ramezani, and M. Newall (2007), Geochronologic constraints on the chronostratigraphic framework of the Neoproterozoic Huqf Supergroup, Sultanate of Oman, *Am. J. Sci.*, *307*, 1097–1145.
Buchan, K., S. Mertanen, R. Park, L. Pesonen, S.-Å. Elming, N. Abrahamsen, and G. Bylund (2000), Comparing the drift of Laurentia and Baltica in the Proterozoic: The importance of key palaeomagnetic poles, *Tectonophysics*, *319*(3), 167–198.
Carazzo, G., and A. Jellinek (2013), Particle sedimentation and diffusive convection in volcanic ash-clouds, *J. Geophys. Res. Solid Earth*, *118*, 1420–1437, doi:10.1002/jgrb.50155.
Chin, M., D. J. Jacob, G. M. Gardner, M. S. Foreman-Fowler, P. A. Spiro, and D. L. Savoie (1996), A global three-dimensional model of tropospheric sulfate, *J. Geophys. Res.*, *101*(D13), 18,667–18,690.
Clough, S., F. Kneizys, and R. Davies (1989), Line shape and the water vapor continuum, *Atmos. Res.*, *23*(3-4), 229–241.
Cox, G. M., C. F. Roots, G. P. Halverson, W. G. Minarik, F. A. Macdonald, and L. Hubert-Theou (2013), Mount Harper Volcanic Complex, Ogilvie Mountains: A far-flung occurrence of the Franklin igneous event, in *Yukon Exploration and Geology 2012*, edited by K. E. MacFarlane, M. G. Nordling, and P. J. Sack, pp. 19–36, Yukon Geological Survey, Whitehorse, Yukon.
Cox, G. M., J. V. Strauss, G. P. Halverson, M. D. Schmitz, W. C. McClelland, R. S. Stevenson, and F. A. Macdonald (2015), Kikiktat Volcanics of Arctic Alaska—Melting of harzburgitic mantle associated with the Franklin Large Igneous Province, *Lithosphere*, *7*, 275–295, doi:10.1130/L435.1.
Cox, G. M., G. P. Halverson, R. S. Stevenson, M. Vokaty, A. Poirier, M. Kunzmann, Z.-X. Li, F. O. Dudas, J. V. Strauss, and F. A. Macdonald (2016), A basalt weathering trigger for Snowball Earth, *Earth Planet. Sci. Lett.*, *446*, 89–99.
Denyszyn, S. W., D. W. Davis, and H. C. Halls (2009a), Paleomagnetism and U-Pb geochronology of the Clarence Head dykes, Arctic Canada: Orthogonal emplacement of mafic dykes in a large igneous province, *Can. J. Earth Sci.*, *46*, 155–167.
Denyszyn, S. W., H. C. Halls, D. W. Davis, and D. A. D. Evans (2009b), Paleomagnetism and U-Pb geochronology of Franklin dykes in High Arctic Canada and Greenland: A revised age and paleomagnetic pole for constraining block rotations in the Nares Strait region, *Can. J. Earth Sci.*, *46*, 689–705.
Dhomse, S., K. Emmerson, G. Mann, N. Bellouin, K. Carslaw, M. Chipperfield, R. Hommel, N. Abraham, P. Telford, and P. Braesicke (2014), Aerosol microphysics simulations of the Mt. Pinatubo eruption with the UM-UKCA composition-climate model, *Atmos. Chem. Phys.*, *14*(20), 11,221–11,246.
Dostal, J., W. R. A. Baragar, and C. Dupuy (1986), Petrogenesis of the Natkusiak continental basalts, Victoria Island, Northwest Territories, Canada, *Can. J. Earth Sci.*, *23*, 622–632.
Ernst, R. E., et al. (2016), Long-lived connection between southern Siberia and northern Laurentia in the Proterozoic, *Nat. Geosci.*, *9*, 464–469.
Evans, D. A. (2006), Proterozoic low orbital obliquity and axial-dipolar geomagnetic field from evaporite palaeolatitudes, *Nature*, *444*, 51–55.
Fanning, C. M., and P. K. Link (2004), U-Pb SHRIMP ages of Neoproterozoic (Sturtian) glaciogenic Pocatello Formation, *Geology*, *32*, 881–884.
Feulner, G. (2012), The faint young Sun problem, *Rev. Geophys.*, *50*, doi:10.1029/2011RG000375.
Feulner, G., C. Hallmann, and H. Kienert (2015), Snowball cooling after algal rise, *Nat. Geosci.*, *8*, 659–662.
Ganino, C., and N. T. Arndt (2009), Climate changes caused by degassing of sediments during the emplacement of large igneous provinces, *Geology*, *37*, 323–326.
Glaze, L. S., and S. M. Baloga (1996), Sensitivity of buoyant plume heights to ambient atmospheric conditions: Implications for volcanic eruption columns, *J. Geophys. Res.*, *101*(D1), 1529–1540, doi:10.1029/95JD03071.
Glaze, L. S., S. Self, A. Schmidt, and S. J. Hunter (2017), Assessing eruption column height in ancient flood basalt eruptions, *Earth Planet. Sci. Lett.*, *457*, 263–270.
Godderis, Y., Y. Donnadieu, A. Nedelec, B. Dupre, C. Dessert, A. Grard, G. Ramstein, and L. M. Francois (2003), The Sturtian 'snowball' glaciation: fire and ice, *Earth Planet. Sci. Lett.*, *6648*, 1–12.
Goldblatt, C., and K. Zahnle (2010), Clouds and the Faint Young Sun Paradox, *Clim. Past Discuss.*, *6*.
Grant, W. B., E. V. Browell, C. S. Long, L. L. Stowe, R. Grainger, and A. Lambert (1996), Use of volcanic aerosols to study the tropical stratospheric reservoir, *J. Geophys. Res.*, *101*(D2), 3973–3988.
Hansen, J. E., and L. D. Travis (1974), Light scattering in planetary atmospheres, *Space Sci. Rev.*, *16*(4), 527–610.
Hartmann, D. L. (2015), Global physical climatology, Newnes.
Heaman, L. M., A. N. LeCheminant, and R. H. Rainbird (1992), Nature and timing of Franklin igneous events, Canada: Implications for a Late Proterozoic mantle plume and the break-up of Laurentia, *Earth Planet. Sci. Lett.*, *109*, 117–131.
Hoffman, P. F., and D. P. Schrag (2002), The snowball Earth hypothesis: Testing the limits of global change, *Terra Nova*, *14*(3), 129–155.
Jacobson, M. Z. (2005), *Fundamentals of Atmospheric Modeling*, Cambridge Univ. Press.
Jacobson, M. Z., R. P. Turco, E. J. Jensen, and O. B. Toon (1994), Modeling coagulation among particles of different composition and size, *Atmos. Environ.*, *28*(7), 1327–1338.
Jefferson, C. W., L. J. Hulbert, R. H. Rainbird, G. E. M. Hall, D. C. Gregoire, and L. I. Grinenko (1994), Mineral resource assessment of the Neoproterozoic Franklin Igneous Events of Arctic Canada: Comparison with the Permo-Triassic Noril'sk-Talnakh Ni-Cu-PGE deposits of Russia, *Geol. Surv. Canada Open File*, *2789*, 48.
Jefferson, C., W. Nelson, R. Kirkham, J. Reedman, and R. Scoates (1985), Geology and copper occurrences of the Natkusiak basalts, Victoria Island, District of Franklin, *Current Res. Part A: Geol. Surv. Canada Pap.*, 203–214.
Kasting, J. F., D. P. Whitmire, and R. T. Reynolds (1993), Habitable zones around main sequence stars, *Icarus*, *101*(1), 108–128.
Kulmala, M., and A. Laaksonen (1990), Binary nucleation of water–sulfuric acid system: Comparison of classical theories with different H2SO4 saturation vapor pressures, *J. Chem. Phys.*, *93*(1), 696–701.
Lan, Z., X. Li, M. Zhu, Z.-Q. Chen, Q. Zhang, Q. Li, D. Lu, Y. Liu, and G. Tang (2014), A rapid and synchronous initiation of the wide spread Cryogenian glaciations, *Precambrian Res.*, *255*, 401–411.
Lan, Z., X.-H. Li, Q. Zhang, and Q.-L. Li (2015), Global synchronous initiation of the 2nd episode of Sturtian glaciation: SIMS zircon U–Pb and O isotope evidence from the Jiangkou Group, South China, *Precambrian Res.*, *267*, 28–38.
Li, Z.-X.,. E. D. A. D., and G. P. Halverson (2013), Neoproterozoic glaciations in a revised global palaeogeography from the breakup of Rodinia to the assembly of Gondwanaland, *Sediment. Geology*, *294*, 219–232.
Liou, K.-N. (2002), *An Introduction to Atmospheric Radiation*, Academic Press.

Macdonald, F. A., M. D. Schmitz, J. L. Crowley, C. F. Roots, D. S. Jones, A. C. Maloof, J. V. Strauss, P. A. Cohen, D. T. Johnston, and D. P. Schrag (2010), Calibrating the Cryogenian, *Science*, *327*, 1241–1243.

Macdonald, F. A., E. F. Smith, J. V. Strauss, G. M. Cox, G. P. Halverson, and C. F. Roots (2011), Neoproterozoic and early Paleozoic correlations in the western Ogilvie Moutnains, Yukon, in *Yukon Exploration and Geology 2010*, edited by K. E. MacFarlane, L. H. Weston, and C. Relf, pp. 161–182, Yukon Geological Survey, Whitehorse.

Maher, K., and C. Chamberlain (2014), Hydrologic regulation of chemical weathering and the geologic carbon cycle, *Science*, *343*, 1502–1504.

Manabe, S., and R. T. Wetherald (1967), Thermal equilibrium of the atmosphere with a given distribution of relative humidity, *J. Atmos. Sci.*, *24*(241).

Marshall, H., J. C. G. Walker, and W. Kuhn (1988), Long-term climate change and the geochmical cycle of carbon, *J. Geophys. Res.*, *93*, 791–801, doi:10.1029/JD093iD01p00791.

McCormick, M. P., L. W. Thomason, and C. R. Trepte (1995), Atmospheric effects of the Mt Pinatubo eruption, *Nature*, *373*(6513), 399–404.

McKenzie, N. R., B. K. Horton, S. E. Loomis, D. F. Stockli, N. J. Planavsky, and C.-T. A. Lee (2016), Continental arc volcanism as the principal driver of icehouse-greenhouse variability, *Science*, *352*(6284), 444–447.

Meador, W., and W. Weaver (1980), Two-stream approximations to radiative transfer in planetary atmospheres: A unified description of existing methods and a new improvement, *J. Atmos. Sci.*, *37*(3), 630–643.

Mills, B., A. J. Watson, C. Goldblatt, R. Boyle, and T. M. Lenton (2011), Timing of Neoproterozoic glaciations linked to transport-limited global weathering, *Nat. Geosci.*, *4*, 861–864.

Morton, B. R., G. Taylor, and J. S. Turner (1956), Proceedings of the Royal Society of London A: Mathematical, physical and engineering sciences, *234*, 1-23.

Mustard, P. S., and C. F. Roots (1997), Rift-related volcanism, sedimentation, and tectonic setting of the Mount Harper Group, Ogilvie Mountains, Yukon Territory, *Geol. Surv. Canada Bull.*, *492*, –0-92.

Myhre, G., E. J. Highwood, K. P. Shine, and F. Stordal (1998), New estimates of radiative forcing due to well mixed greenhouse gases, *Geophys. Res. Lett.*, *25*(14), 2715–2718, doi:10.1029/98GL01908.

Nabelek, P. I., J. H. Bédard, and R. H. Rainbird (2014), Numerical constraints on degassing of metamorphic CO2 during the Neoproterozoic Franklin large igneous event, Arctic Canada, *Geol. Soc. Am. Bull.*, *126*(5–6), 759–772.

Neu, J. L., and R. A. Plumb (1999), Age of air in a "leaky pipe" model of stratospheric transport, *J. Geophys. Res.*, *104*(D16), 19,243–19,255.

Newton, R. C., and C. E. Manning (2005), Solubility of anhydrite, CaSO4, in NaCl–H2O solutions at high pressures and temperatures: Applications to fluid–rock interaction, *J. Petrol.*, *46*, 701–716.

Pehrsson, S. J., and K. L. Buchan (1999), Borden dykes of Baffin Island, Northwest Territories: A Franklin U-Pb baddelyite age and paleomagnetic reinterpretation, *Can. J. Earth Sci.*, *36*, 65–73.

Pierrehumbert, R. T. (2011), *Principles of Planetary Climate*, Cambridge University Press.

Pierrehumbert, R., D. Abbot, A. Voigt, and D. Koll (2011), Climate of the Neoproterozoic, *Annu. Rev. Earth Planet. Sci.*, *39*, 417.

Pinto, J. P., R. P. Turco, and O. B. Toon (1989), Self-limiting physical and chemical effects in volcanic eruption clouds, *J. Geophys. Res.*, *94*(D8), 11,165–11,174.

Rainbird, R. H. (1993), The sedimentary record of mantle plume uplift preceding eruption of the Neoproterozoic Natkusiak flood basalt, *J. Geol.*, *101*, 305–318.

Rasch, P. J., S. Tilmes, R. P. Turco, A. Robock, L. Oman, C.-C. J. Chen, G. L. Stenchikov, and R. R. Garcia (2008), An overview of geoengineering of climate using stratospheric sulphate aerosols, *Philos. Trans. R. Soc. London, Ser. A*, *366*, 4007–4037.

Read, W., L. Froidevaux, and J. Waters (1993), Microwave limb sounder measurement of stratospheric SO2 from the Mt. Pinatubo volcano, *Geophys. Res. Lett.*, *20*(12), 1299–1302, doi:10.1029/93GL00831.

Robertson, J., E. M. Ripley, S. J. Barnes, and C. Li (2015), Sulfur liberation from country rocks and incorporation in mafic magmas, *Econ. Geol.*, *110*, 1111–1123.

Rooney, A. D., F. A. Macdonald, J. V. Strauss, F. O. Dudas, C. Hallman, and D. Selby (2014), Re-Os geochronology and coupled Os-Sr isotope constraints on the Sturtian snowball Earth, *Proc. Natl. Acad. Sci.*, *1073*, 1–6.

Rooney, A. D., J. V. Strauss, A. D. Brandon, and F. A. Macdonald (2015), A Cryogenian chronology: Two long-lasting, synchronous Neoproterozoic Snowball Earth glaciations, *Geology*, *43*, 459–462.

Russell, P., J. Livingston, R. Pueschel, J. Bauman, J. Pollack, S. Brooks, P. Hamill, L. Thomason, L. Stowe, and T. Deshler (1996), Global to microscale evolution of the Pinatubo volcanic aerosol derived from diverse measurements and analyses, *J. Geophys. Res.*, *101*(D13), 18,745–18,763.

Sander, S., D. Golden, M. Kurylo, G. Moortgat, P. Wine, A. Ravishankara, C. Kolb, M. Molina, B. Finlayson-Pitts, and R. Huie (2006), Chemical kinetics and photochemical data for use in atmospheric studies evaluation number 15, Rep., Jet Propul. Lab., National Aeronautics and Space Administration, Pasadena, Calif.

Schoene, B., J. C. Crowley, D. J. Condon, M. D. Schmitz, and S. A. Bowring (2006), Reassessing the uranium decay constants for geochronology using ID-TIMS U–Pb data, *Geochim. Cosmochim. Acta*, *70*, 426–445.

Schoene, B., J. Guex, A. Bartolini, U. Schaltegger, and T. J. Blackburn (2010), Correlating the end-Triassic mass extinction and flood basalt volcanism at the 100 ka level, *Geology*, *38*, 387–390.

Schrag, D. P., R. A. Berner, P. F. Hoffman, and G. P. Halverson (2002), On the initiation of snowball Earth, *Geochem. Geophys. Geosyst.*, *3*, 1–21, doi:10.1029/2001GC000219.

Segura, A., K. Krelove, J. F. Kasting, D. Sommerlatt, V. Meadows, D. Crisp, M. Cohen, and E. Mlawer (2003), Ozone concentrations and ultraviolet fluxes on Earth-like planets around other stars, *Astrobiology*, *3*(4), 689–708.

Seinfeld, J. H., and S. N. Pandis (2016), *Atmospheric Chemistry and Physics: From Air Pollution to Climate Change*, John Wiley.

Self, S., T. Thordarson, and M. Widdowson (2005), Gas fluxes from flood basalt eruptions, *Elements*, *1*, 283–287.

Self, S., M. Widdowson, T. Thordarson, and A. E. Jay (2006), Volatile fluxes during flood basalt eruptions and potential effects on the global environment: A Deccan perspective, *Earth Planet. Sci. Lett.*, *248*, 518–532.

Self, S., A. Schmidt, and T. Mather (2014), Emplacement characteristics, time scales, and volcanic gas release rates of continental flood basalt eruptions on Earth, *Geol. Soc. Am. Spec. Pap.*, *505*, SPE505–SPE516.

Serdyuchenko, A., V. Gorshelev, M. Weber, W. Chehade, and J. Burrows (2014), High spectral resolution ozone absorption cross-sections–Part 2: Temperature dependence, *Atmos. Meas. Tech.*, *7*, 625–636.

Sloan, L. C., and D. Rea (1996), Atmospheric carbon dioxide and early Eocene climate: A general circulation modeling sensitivity study, *Palaeogeogr. Palaeoclimatol. Palaeoecol.*, *119*(3), 275–292.

Stern, R. J., D. Avigad, N. Miller, and M. Beyth (2008), From volcanic winter to Snowball Earth: An alternative explanation for Neoproterozoic biosphere stress, in *Links Between Geological Processes, Microbial Activities&Evolution of Life*, pp. 313–337, Springer.

Stothers, R. B., J. A. Wolff, S. Self, and M. R. Rampino (1986), Basaltic fissure eruptions, plume heights, and atmospheric aerosols, *Geophys. Res. Lett.*, *13*(8), 725–728, doi:10.1029/GL013i008p00725.
Strauss, J. V., A. D. Rooney, F. A. Macdonald, A. D. Brandon, and A. H. Knoll (2014), 740 Ma vase-shaped microfossils from Yukon, Canada: Implications for Neoproterozoic chronology and biostratigraphy, *Geology*, *G35736*, 35,731.
Taylor, E. L., T. N. Taylor, and N. R. Cúneo (1992), The present is not the key to the past: A polar forest from the Permian of Antarctica, *Science*, 1675–1675.
Telling, J., and J. Dufek (2012), An experimental evaluation of ash aggregation in explosive volcanic eruptions, *J. Volcanol. Geotherm. Res.*, *209*, 1–8.
Textor, C., H. F. Graf, M. Herzog, and J. Oberhuber (2003), Injection of gases into the stratosphere by explosive volcanic eruptions, *J. Geophys. Res.*, *108*(D19), doi:10.1029/2002JD002987.
Thibodeau, A. M., and B. A. Bergquist (2017), Do mercury isotopes record the signature of massive volcanism in marine sedimentary records?, *Geology*, *45*(1), 95–96.
Thordarson, T., and S. Self (1996), Sulfur, chlorine and fluorine degassing and atmospheric loading by the Roza eruption, Columbia River Basalt Group, Washington, USA, *J. Volcanol. Geotherm. Res.*, *74*(1), 49–73.
Thordarson, T., and S. Self (1998), The Roza Member, Columbia River Basalt Group: A gigantic pahoehoe lava flow field formed by endogenous processes?, *J. Geophys. Res.*, *103*(B11), 27,411–27,445.
Thordarson, T., and S. Self (2003), Atmospheric and environmental effects of the 1783–1784 Laki eruption: A review and reassessment, *J. Geophys. Res.*, *108*(D1), doi:10.1029/2001JD002042.
Thordarson, T., S. Self, N. Oskarsson, and T. Hulsebosch (1996), Sulfur, chlorine, and fluorine degassing and atmospheric loading by the 1783–1784 AD Laki (Skaftár Fires) eruption in Iceland, *Bull. Volcanol.*, *58*(2–3), 205–225.
Thordarson, T., S. Self, D. Miller, G. Larsen, and E. Vilmundardóttir (2003), Sulphur release from flood lava eruptions in the Veidivötn, Grímsvötn and Katla volcanic systems, Iceland, *Geol. Soc. London, Spec. Publ.*, *213*(1), 103–121.
Tisdale, R. T., D. L. Glandorf, M. A. Tolbert, and O. B. Toon (1998), Infrared optical constants of low-temperature H2SO4 solutions representative of stratospheric sulfate aerosols, *J. Geophys. Res.*, *103*(D19), 25,353–25,370.
Tollo, R. P., and J. N. Aleinikoff (1996), Petrology and U-PB geochronology of the Robertson River Igneous Suite, Blue Ridge province, Virginia—Evidence for multistage magmatism associated witn an early episode of Laurentian rifting, *Am. J. Sci.*, *296*(9), 1045–1090.
Turco, R., P. Hamill, O. Toon, R. Whitten, and C. Kiang (1979a), A one-dimensional model describing aerosol formation and evolution in the stratosphere: I. Physical processes and mathematical analogs, *J. Atmos. Sci.*, *36*(4), 699–717.
Turco, R., P. Hamill, O. Toon, R. Whitten, and C. Kiang (1979b), The NASA-AMES Research Center stratospheric aerosol model. 1. Physical processes and computational analogs.
Tziperman, E., I. Halevy, D. T. Johnston, A. H. Knoll, and D. P. Schrag (2011), Biologically induced initiation of Neoproterozoic snowball-Earth events, *Proc. Natl. Acad. Sci.*, *108*, 15,091–15,096.
Voigt, A., and J. Marotzke (2010), The transition from the present-day climate to a modern Snowball Earth, *Clim. Dyn.*, *35*, 887–905.
Voigt, A., D. Abbot, R. Pierrehumbert, and J. Marotzke (2011), Initiation of a Marnoun Snowball Earth in a state-of-the-art atmosphere-ocean general circulation model, *Clim. Past*, *7*, 249–263.
Volk, C., J. Elkins, D. Fahey, and R. Salawitch (1996), Quantifying transport between the tropical and mid-latitude lower stratosphere, *Science*, *272*(5269), 1763.
Williamson, N. M., L. Ootes, R. H. Rainbird, J. H. Bédard, and B. Cousens (2016), Initiation and early evolution of the Franklin magmatic event preserved in the 720 Ma Natkusiak Formation, Victoria Island, Canadian Arctic, *Bull. Volcanol.*, *78*, 1–19.
Wordsworth, R., and R. Pierrehumbert (2013a), Water loss from terrestrial planets with CO2-rich atmospheres, *Astrophys. J.*, *778*, 154.
Wordsworth, R., and R. Pierrehumbert (2013b), Hydrogen-nitrogen greenhouse warming in Earth's early atmosphere, *Science*, *339*, 64–67.
Wordsworth, R., F. Forget, and V. Eymet (2010), Infrared collision-induced and far-line absorption in dense CO 2 atmospheres, *Icarus*, *210*, 992–997.
Wordsworth, R., F. Forget, E. Millour, J. Head, J. Madeleine, and B. Charnay (2013), Global modelling of the early Martian climate under a denser CO 2 atmosphere: Water cycle and ice evolution, *Icarus*, *222*, 1–19.
Wunsch, C., and R. Ferrari (2004), Vertical mixing, energy, and the general circulation of the oceans, *Annu. Rev. Fluid Mech.*, *36*, 281–314.
Xu, B., S. Xiao, H.-B. Zou, Y. Chen, Z.-X. Li, B. Song, D.-Y. Liu, C.-M. Zhou, and X.-L. Yuan (2009), SHRIMP zircon U-Pb age constraints on Neoproterozoic Quruqtah diamictites in NW China, *Precambrian Res.*, *168*, 247–258.
Yang, J., W. Peltier, and Y. Hu (2012), The initiation of modern soft and hard Snowball Earth climates in CCSM4, *Clim. Past*, *8*, 907–918.
Young, G. M. (1981), The Amundsen Embayment, Northwest Territories: Relevance to the Upper Proterozoic evolution of North America, in *Proterozoic Basins of Canada*, edited by F. H. A. Campbell, pp. 203–218, *Geol. Surv. Canada Pap.*, *81-10*.
Zhang, Q.-R., X.-H. Li, L.-J. Feng, J. Huang, and S. Biao (2008), A new age constraint on the onset of the Neoproterozoic glaciations in the Yangtze Platform, South China, *J. Geol.*, *116*, 423–429.
Zhang, S., D. A. Evans, H. Li, H. Wu, G. Jiang, J. Dong, Q. Zhao, T. D. Raub, and T. Yang (2013), Paleomagnetism of the late Cryogenian Nantuo Formation and paleogeographic implications for the South China Block, *J. Asian Earth Sci.*, *72*, 164–177.

Supporting Information for "Initiation of Neoproterozoic Snowball Earth with volcanic sulfur aerosol emissions"

F. Macdonald[1] and R. Wordsworth[1,2]

1. Materials and Methods

1.1. Geological Setting

Igneous rocks associated with the Franklin LIP are dominated by mafic dikes and sills that intrude the Canadian Shield and Proterozoic basins on the Arctic margin of Laurentia (Fig. 1A in main text), and may be correlative with similar aged intrusions on the southern margin of Siberia [*Ernst et al.*, 2016]. The dikes presumably fed large basaltic

---

Corresponding author: Robin Wordsworth, School of Engineering and Applied Sciences, Harvard University, Cambridge, MA 02138. (rwordsworth@seas.harvard.edu)

[1]Department of Earth and Planetary Sciences, Harvard University, Cambridge, MA 02138, USA

[2]School of Engineering and Applied Sciences, Harvard University, Cambridge, MA 02138, USA

provinces that have since been largely eroded. Preserved extrusive volcanic rocks include the Natkusiak Formation basalt of Minto Inlier, Victoria Island [*Dostal et al.*, 1986; *Jefferson et al.*, 1985], the Mount Harper Volcanics of the Coal Creek inlier in the Ogilvie Mountains [*Cox et al.*, 2013; *Mustard and Roots*, 1997], Yukon, the Pleasant Creek Volcanics of the Tatonduk inlier, which straddles the Yukon-Alaska border [*Macdonald et al.*, 2011], and the Kikiktak Volcanics of Arctic Alaska [*Cox et al.*, 2015]. These extrusive rocks are composed predominantly of tholeitic basalt to basaltic andesites, typical of continental flood basalts.

The Natkusiak magmatic assemblage consists of dolerite sills that intruded the Shaler Supergroup [*Young*, 1981; *Rainbird*, 1993], northwesterly striking dikes, and a succession of plateau basalts [*Dostal et al.*, 1986]. Sedimentary strata of the underlying Shaler Supergroup were updomed, beveled and faulted before and during the emplacement of the Natkusiak magmatic assemblage [*Rainbird*, 1993; *Bedard et al.*, 2012]. Sills range in thickness from 5 to 100 m; some are differentiated with olivine accumulation at their base and pegmatites in their upper levels [*Dostal et al.*, 1986]. Exposures of the Natkusiak Formation basalts have been separated into a northern lobe [*Jefferson et al.*, 1985] and a southern lobe [*Williamson et al.*, 2016] of exposures preserved in synclines. The Natkusiak Formation basalts are thickest in the northern lobe, with a maximum preserved thickness of $\sim$ 1100 m, and has been divided into seven members [*Jefferson et al.*, 1985]. In the southern lobe, the Natkusiak Formation is up to 200 m thick and has been separated into four units that have been correlated with Jefferson et al.'s (1985) 'basal member', 'pyroclastic member', and 'lower massive member in the northern lobe [*Williamson et al.*,

2016]. Thus, it appears that units above the 'Lower Massive Member' in the northern lobe are not preserved in the southern lobe.

Nabelek et al. [2014] estimated the amount of metamorphic CO_2 released from the emplacement of the gabbroic sills associated with the Franklin LIP into carbonate strata of the Shaler Supergroup. Along with carbonate, the Shaler Supergroup includes organic rich shale and evaporite deposits at multiple horizons that are several tens of meters thick. *Evans* [2006] estimated a volume of 30,000 km^3 in the upper evaporites of the Kilian-Redstone River deposits and 90,000 km^3 in the lower evaporites of the Minto Inlet Formation. Although the total amount and rate of S release during the emplacement of sills in the Shaler Supergroup is poorly constrained, disseminated copper sulfides are present within basalt flows, outlining clasts in the pyroclastic member, and as veins in all of the members [*Jefferson et al.*, 1985]. Additionally, many of the sills and dikes have extremely high sulfur concentrations [*Jefferson et al.*, 1994; *Bedard et al.*, 2016]. Although dikes have been observed that feed the sills, feeder dikes for the basalts have not been observed. Yet, it is assumed that at least some of the dikes fed the basalts as is suggested by their similar chemistry [*Dostal et al.*, 1986; *Heaman et al.*, 1992]. Some of the sills are folded around a volcanic center near Kilian Lake that has been correlated with the pyroclastic member [*Jefferson et al.*, 1994], suggesting that at least some of the sills formed before or very early in the eruption sequence. However, other sills are vesiculated and feed flows higher in the basaltic stack. Although fissure eruption centers have not been identified associated with the Franklin, the exposure is limited and it does not mean they

were not there, and several circular to keyhole shaped eruption centers have been mapped [the largest one identified is $\sim 3 \times 2$ km [*Jefferson et al.*, 1994]].

Paleomagnetic data from the Franklin LIP provide the most robust Neoproterozoic pole for Laurentia and is an important tie point for Neoproterozoic paleogeography [*Buchan et al.*, 2000]. Data spanning six key regions, the Canadian Mainland, Victoria Island, Baffin Island, Devon Island, Ellesmere Island and northern Greenland, yield a grand mean pole that restores Laurentia and the Natkusiak assemblage of the Franklin LIP at ca. 717 Ma to within 9 degrees of the equator [*Buchan et al.*, 2000; *Denyszyn et al.*, 2009a] (Fig. 1A in main text).

U-Pb zircon and baddeleyite ages from the Franklin LIP rocks span ca. 725-710 Ma (Table S1). This spread could represent distinct pulses of magmatism; however, for younger, better dated LIPs, most of the volume is erupted in $<<$ 1 Myr [*Self et al.*, 2014]. Instead, this large spread may also be due to imprecise multigrain techniques and upper intercept ages, and we suggest that the most precise dates represent the best age constraint on the Franklin LIP. The most precise, single grain chemical abrasion-isotope dilution-thermal ion mass spectrometry (CA-ID-TIMS) on zircon and baddeleyite associated with the Franklin LIP yield ages between 717 and 716 Ma (Table S1). It has been also proposed that the ca. 725 Ma Dovyren Intrusive Complex in the Lake Baikal region of Russia represents a component of the Franklin LIP in SW Siberia [*Ernst et al.*, 2016]. If true it would provide evidence that Franklin magmatism initiated well before the onset of the Sturtian glaciation and covered an area beyond that defined by the radiating dyke swarm

in north-central to northeastern Laurentia. However, the Siberian age is imprecise and hence this correlation remains speculative.

A quartz-rich rhyolite flow in member D of the Mount Harper Volcanics was dated at 717.4 ± 0.2 Ma and a tuff interfingering with glacial deposits of the overlying Rapitan Group was dated at 716.5 ± 0.2 Ma, both with U-Pb CA-ID TIMS on zircon [*Macdonald et al.*, 2010]. These dates have been interpreted to bracket the onset of the Sturtian glaciation [*Macdonald et al.*, 2010]. Additional recent ages on the Franklin LIP and the onset of the Sturtian glaciation confirm this age model (Table S1). In China, an ash bed within stratified diamictite of the lowermost Chang-an Formation was dated with secondary ion mass spectrometry (SIMS) on zircon at 715.9 ± 2.8 Ma [*Lan et al.*, 2014a]. In Arctic Alaska, a 719.5 ± 0.3 Ma CA-ID-TIMS age on zircon from volcaniclastic strata at the top of the Kikiktak Volcanics and directly below the Hula Hula diamictite is consistent with both a Sturtian-age of the Hula Hula diamictite and a tight temporal relationship between the Franklin LIP and the onset of the Sturtian glaciation[*Cox et al.*, 2015]. Sills that intrude evaporite rich-strata of the upper Shaler Supergroup dated at 716.3 ± 0.5 Ma (ID-TIMS on baddelyite) [*Macdonald et al.*, 2010] are indistinguishable from the constraints on the onset of the Sturtian glaciation (Fig. 1 in the main text). Importantly, the dated sill, sill 6a near Kilim Lake, is one of most sulfur-rich sills analysed to date [*Jefferson et al.*, 1985].

1.2. Geochemistry

Subaerial continental flood basalt (CFB) volcanism is characterized by the repeated effusion of $\sim 10^3$ km^3 of basaltic magma in less than 1 Myr. Each eruption comes from a

dyke-fed fissure and can last up to a decade or more [*Self et al.*, 2014]. During eruptions, gas fluxes of > 1 Gt per year of SO_2 and CO_2 are possible [*Self et al.*, 2005]. These volumes can increase when magmatic systems invade volatile-rich sediments as more volatiles are entrained into the melt. The occurrence of spatter, spatter-fed lava, and scoria mounds along eruptive fissures in the Columbia River CFB and in Icelandic fissure eruptions suggests the occurrence of violent fire-fountaining events [*Self et al.*, 2006]. It has been estimated that these fire fountains exceeded 1.5 km in height with convective plumes rising to heights in excess of 13 km [*Self et al.*, 2005].

Estimates of gas-release budgets with melt inclusion studies are limited to individual CFB eruptions in the mid-Miocene Columbia River CFB [*Thordarson and Self*, 1996], the Deccan Traps [*Self et al.*, 2005], Siberian Traps [*Black et al.*, 2012], and studies of Icelandic fissure eruptions [*Thordarson et al.*, 1996]. These studies suggest that $\sim$75% of volative S species present in the rising melt are released at the vents largely as SO_2 [*Self et al.*, 2005]. The months-long Laki eruption in Iceland is estimated to have released $\sim$120 Mt of SO_2 with maximum fluxes reaching 6 Mt per day [*Thordarson et al.*, 1996]. Estimation of S gas release from ancient eruptions is compromised by weathering and ground water alteration, which leads to the removal of volatile elements. Nonetheless, using melt inclusions it has been estimated that a single flow with in the Columbia CFB released $\sim$12 Gt of SO_2 [*Thordarson and Self*, 1996]. Melt inclusion studies are beyond the scope of this study and it is not clear that there is material preserved in the Franklin LIP that is pristine enough for such a study.

In crystal-poor or altered CFBs, original S content of the lava can be estimated with the S content of undegassed dikes and sills normalized to TiO_2/FeO_2 [*Thordarson et al.*, 2003]. S saturated melts from LIPs typically have between 1000 and 2500 ppm of S prior to degassing and flows contain much lower concentrations between 200 and 300 ppm [*Self et al.*, 2005]. Major, minor, and trace element concentrations including S concentrations and S isotopes from sills and dikes associated with the Franklin LIP were compiled by *Bedard et al.* [2016]. S concentrations in sills range from 100-100,000 ppm and S isotopes show increasing variability with increasing concentration indicative of wall-rock assimilation (Fig. S1). At these high S concentrations, and with the late addition of S out of equilibrium with the melt, normalization of S concentrations to TiO_2/FeO_2 is both insignificant and not appropriate. If we assume ∼75% of S remains in melt [*Self et al.*, 2005], and that the sills were variably degassed from original S concentrations less than 2500 ppm, the upper end of this range is greater than that of basaltic flows in the Columbia River CFB [*Thordarson and Self*, 1996], the Deccan Traps [*Self et al.*, 2005], Siberian Traps [*Black et al.*, 2012], and the Icelandic fissure eruptions [*Thordarson et al.*, 1996].

Crustal S is incorporated into mafic magmas predominantly via direct melting and assimilation of wall rock and xenoliths rather than by the liberation of sulfur during contact metamorphism in the thermal aureole [*Robertson et al.*, 2015]. Although previous work has questioned the viability of releasing sulfur via intrusions into evaporites due to the high melting temperature of pure anhydrite (∼1450°C), the melting temperature of mixtures of anhydrite and dolomite, which is probably closer to the composition of the wall

rock intruded by the Natkusiak sills, is much lower (∼1000°C) [*Robertson et al.*, 2015]. Moreover, hydrothermal systems associated with the Franklin LIP may have partially dissolved the evaporites, and if these fluids were saline, the solubility of anhydrite greatly increases with NaCl activity at temperatures between 600° and 800°C [*Newton and Manning*, 2005]. We suggest that excess S was incorporated into magmas primarily through the melting and dissolution of evaporite layers in the Minto Inlier and Killian formations of the Shaler Supergroup when intruded by sills, and then was rapidly degassed as bubbles in shallow intrusions, fissure eruptions, and in flows that were fed by these sills.

Petrographic analysis has revealed abundant disseminated pyrite and immiscible metallic sulfur in the sills. Bulk S isotope studies preserve a wide range of compositions (Fig. S1), differing from the value of mantle derived LIPs (∼ 0‰ VCDT). Although *Jefferson et al.* [1994] argued that trace element compositions suggest that the sulfur was sourced from sulfidic shale of the Wynniatt Fm, the high S concentrations and the enriched S isotopic values of several of the sills are consistent with the S also coming from the entrainment of carbonate and sulfur evaporates into the sills (Fig. S1). However, because we are concerned with decadal fluxes of SO_2, the source and the total amount of S entrained and released in magmatic system are not critical. What is important is that the sills that are coincident with the onset of the Sturtian glaciation contain considerably more S than typical CFBs.

1.3. Radiative-convective climate model

To estimate the climate effect of Franklin LIP eruptions, we combine radiative-convective, aerosol microphysics and volcanic plume modeling tools. In the following sections, each of these components is described in detail.

To calculate Neoproterozoic tropopause height, we used a 1D radiative-convective model. The model atmospheric temperature structure is calculated as a function of surface temperature assuming adjustment to a moist adiabat in the troposphere, following the methodology in *Wordsworth and Pierrehumbert* [2013]. The tropopause height is then defined using the standard Earth-based empirical measure as where the magnitude of the vertical temperature gradient drops below 2 K/km ($dT/dz > -2$ K/km). To relate CO_2 molar concentration to surface temperature, we performed iterative 1D radiative-convective calculations with moist adjustment in the troposphere and an assumed relative humidity of 0.77 [*Manabe and Wetherald*, 1967]. In the stratosphere, the temperature profile is allowed to evolve freely until thermal equilibrium is reached.

Atmospheric radiative transfer is calculated using a correlated-k approach [*Wordsworth et al.*, 2013]. The absorption effects of CO_2 and H_2O (infrared and visible) and O_3 (UV) are taken into account; absorption by other gases is set to zero. Rayleigh scattering in the shortwave by N_2 and O_2 is taken into account, but the radiative effects of clouds are neglected. The surface albedo is set to 0.24, a value that allows the model to reproduce the present-day mean surface temperature (288 K) in simulations with present-day solar flux, surface pressure and atmospheric composition. Such an elevated surface albedo implicitly accounts for the effect of low-lying clouds (a standard assumption in

1D radiative-convective modelling). The radiative forcing due to clouds is uncertain in Earth's paleoclimate [*Goldblatt and Zahnle*, 2010; *Sloan and Rea*, 1996], so inclusion of a fixed cloud forcing here would not have led to greater insight.

For the CO_2 and H_2O line absorption, we computed high resolution spectra over a range of temperatures, pressures and gas mixing ratios. We used an $6 \times 8 \times 8$ temperature, pressure and H_2O molar concentration grid with values $T = \{100, 150, \ldots, 350\}$ K, $p = \{10^{-3}, 10^{-2}, \ldots, 10^{4}\}$ mbar and $f_{H_2O} = \{10^{-8}, 10^{-7}, \ldots, 10^{-1}\}$, respectively. The correlated-k method was used to produce fast coefficients for the radiative-convective simulations, with the CO_2 mixing ratio chosen in advance for each calculation. The H_2O continuum was implemented using the MT-CKD parametrization [*Clough et al.*, 1989; *Pierrehumbert*, 2011]. We used 80 spectral bands in the longwave and 82 in the shortwave, and sixteen points for the g-space integration, where g is the cumulated distribution function of the absorption data for each band. Twelve new bands were added to the shortwave compared to previous studies [*Wordsworth and Pierrehumbert*, 2013] to give sufficient resolution in the ultraviolet to model absorption by ozone accurately.

Ultraviolet O_3 absorption cross-sections are derived from the MPI-Mainz UV/VIS Spectral Atlas [*Serdyuchenko et al.*, 2014] while the solar spectrum is taken from the VPL database [*Segura et al.*, 2003]. Calculations were performed with two O_3 molar concentration profiles: one assumed present-day values, while the other assumed an O_3 profile appropriate to an atmosphere with oxygen levels $1/10^{th}$ of today.

1.4. Aerosol radiative transfer

We use Mie theory to calculate aerosol extinction efficiency, single scattering albedo and asymmetry parameter as a function of wavelength for a given particle size distribution ouput by the microphysical model. The aerosol radiative forcing is calculated using the two-stream approximation, with Eddington scaling used in the shortwave and hemi-isotropic emission assumed in the longwave [*Meador and Weaver*, 1980]. We assume that absorption dominates in the longwave and that scattering dominates in the shortwave. Delta scaling is applied to the shortwave optical coefficients to ensure that the forward peak of the phase function is correctly captured at large particle size parameters. We describe the phase function using the Henyey-Greenstein approximation [*Liou*, 2002]. For the aerosol particle refractive indices, we use the data given in *Tisdale et al.* [1998], which were measured at stratospheric temperatures ($\sim$200 K). Solar zenith angle θ_z was calculated by diurnal and seasonal averaging across the microphysics box domain, with weighting by the instantaneous insolation [*Hartmann*, 2015]. For the equatorial eruption simulations (see next section), this yielded $\theta_z = 43.8°$, while for the midlatitude case the value was $\theta_z = 55.4°$. Finally, for the equatorial eruption simulations shown in Fig. 3A in the main text, we used a pre-aerosol tropical planetary albedo of 0.24. This was obtained by averaging albedo data from the Earth Radiation Budget Experiment (ERBE) mission [*Pierrehumbert*, 2011; *Barkstrom*, 1984] over the simulation domain. The same procedure was used to obtain the albedo value of 0.365 for the second mid-latitude eruption plot in Fig. S8.

1.5. Volcanic plume model

The volcanic plume model simultaneously solves the equations of mass, momentum and energy transport for an axisymmetric, steady-state circular plume that entrains the surrounding air as it rises. These equations are defined as

$$\frac{\mathrm{d}f_1}{\mathrm{d}z} = \frac{\mathrm{d}}{\mathrm{d}z}(\rho_g u r^2) = 2\alpha\rho_a u r \tag{1}$$

$$\frac{\mathrm{d}f_2}{\mathrm{d}z} = \frac{\mathrm{d}}{\mathrm{d}z}(f_1 u) = g(\rho_a - \rho_g)r^2 \tag{2}$$

$$\frac{\mathrm{d}f_3}{\mathrm{d}z} = \frac{\mathrm{d}}{\mathrm{d}z}(f_1 c_{p,g} T_g) = 2\alpha\rho_a u r c_{p,a} T_a - \rho_a u r^2 g. \tag{3}$$

with

$$f_1 = \rho_g u r^2 \tag{4}$$

$$f_2 = f_1 u \tag{5}$$

$$f_3 = f_1 c_{p,g} T_g. \tag{6}$$

Here α is an entrainment coefficient, z is altitude, u is the vertical speed of the plume, r is the plume radius, ρ_a is the density of ambient air, ρ_g is the mean density of gas in the plume, g is gravity, T_a is the local atmospheric temperature, T_g is the plume gas temperature and $c_{p,a}$ and $c_{p,g}$ are the specific heat capacity at constant pressure of ambient air and of the plume gas, respectively. The plume specific heat capacity and gas constant are modified as it moves upwards to account for the entrainment of ambient air.

After boundary conditions at the surface are chosen (see below), (1-3) are integrated upwards until the vertical speed of the plume equals zero. The height at which this occurs is then defined as the maximum plume height. This plume model is based on the methodology of *Glaze and Baloga* [1996]. It is a generalization of the classic incompressible model

of *Morton et al.* [1956], which has been validated via numerous laboratory experiments and comparison with observations of real volcanic eruptions [*Stothers et al.*, 1986]. For the numerical integration upwards we use a simple forward Euler approach, with vertical resolution increased to the point where the results converge (1000 levels here).

To initialize our model, we use the same approach as in a previous study that successfully predicted the plume heights of the historic Laki, Mauna Loa and Askja eruptions [*Stothers et al.*, 1986]. Specifically, we link Q to the volume eruption rate V_{erupt} [m^3/s] via the expression

$$Q = \rho_{magma} V_{erupt}[(1 - q_f - q_v)c_{p,magma}\Delta T_c + (q_f c_{p,magma} + q_v c_{p,v})\Delta T_g]. \quad (7)$$

Equation (8) assumes that the plume is heated by a combination of volatiles, fines and clasts, with a negligible contribution from fire fountain lava blobs. Here ρ_{magma} is the magma density, which we take to be 2900 kg/m^3 — a value appropriate to basaltic composition, q_f is the specific concentration of fines [kg/kg] and q_v is the specific concentration of volatiles. $c_{p,magma}$ and $c_{p,v}$ are the specific heat of magma and volatiles, respectively. ΔT_c is the temperature drop of clasts in the fire fountain while ΔT_g is the temperature drop of volatiles and fines in the plume. See Table S2 for definitions and values of all model parameters.

We assume conservative values for the key unknown parameters: $q_f = 0.01$ kg/kg, $q_v = 0.02$ kg/kg, $\Delta T_c = 50$ K and $\Delta T_g = T_{g,0} - T_{g,1} = 1400 - 220 = 1180$ K (here $T_{g,1}$ is the assumed final plume temperature). We assume the dominant volatile by mass is water vapor. The contribution of sulfur and other comparatively minor species to the heat budget is neglected. The initial mass flux is calculated from the heat flux assuming

a circular vent as in *Glaze and Baloga* [1996]

$$f_{1,0} = \frac{Q}{\pi c_{p,v}(T_{g,0} - T_{a,0})}. \quad (8)$$

where 0 denotes initial (surface) variables. Fissure systems tend to produce lines of circular cones to key-hole shaped vents that range from tens of meters to kilometers in diameter, but more elongated eruptive centers also occur. *Glaze et al.* [2017] found that elongated geometries produce larger plumes, but for simplicity we use a conservative circular geometry here. Finally, a conservatively low initial plume speed of $u_0 = 10$ m/s is assumed. In general, we find low sensitivity of the results to the initial plume speed over wide ranges (up to several hundred m/s) because the initial thermal energy is many times greater.

1.6. Aerosol microphysical model

We model key aspects of the sulfate aerosol microphysics, focusing on those processes that play the most important role in determining total radiative forcing. Our model describes the evolution of SO_2 and H_2SO_4 gas, Aitken particles (aerosol condensation nuclei), and the aerosols themselves. Aerosol particles undergo nucleation onto Aitken particles, growth, sedimentation and coagulation. In the microphysical model, the stratosphere is treated as a single box that exchanges material with the troposphere. The advantage of this idealized approach is that it captures the key processes governing aerosol optical depth and mean radius while allowing rapid exploration of sensitivity to poorly constrained parameters. Given the uncertainties, this approach is a more robust one than using a complex off-the-shelf model tuned to present-day Earth conditions.

Once they reach the tropical stratosphere, sub-tropical transport barriers cause aerosols lofted there to remain mostly confined to that region [*Volk et al.*, 1996; *Neu and Plumb*, 1999]. Orbital observations of stratospheric aerosol loading after Pinatubo showed that aerosol optical depth at 0.5 μm remained above 1/2 the peak value for around 45 weeks, with a strong peak in forcing in the 30°S-30°N latitude region [*McCormick et al.*, 1995; *Grant et al.*, 1996]. Modeling the stratospheric meridional circulation in the Neoproterozoic is challenging due to uncertainties in topographic wave forcing and stratospheric wave-mean interaction, but the aerosol transport following eruptions of the Franklin LIP should have been broadly similar.

In this study we treat the tropical and midlatitude stratosphere as distinct domains. For the tropical eruption simulations shown in the main text, we defined the domain base as 16 km and the domain volume as $V = 2\pi r_E s \Delta z$, with r_E Earth's radius, $s = 1.04 r_E$, corresponding to a latitudinal extent from 30° S to 30° N, and $\Delta z = 15$ km the height of the simulation domain. Our microphysical model is sectional, with 82 particle bins ranging from 0.01 μm to 4.14 μm radius. Bin spacing is defined geometrically, with the particle volume increasing by a factor of 1.25 each time the bin number increases. Once the microphysical model produces aerosol mass loading and size distribution data as a function of time, its results are fed into the radiative transfer model to yield net radiative forcing in the domain. Global net radiative forcing is then calculated by multiplying the results by a factor $2\pi r_E s / 4\pi r_E^2$.

The model prognostic equations take the general form

$$\frac{\partial \tilde{n}_k(t)}{\partial t} = P_k - L_k + \left.\frac{\partial \tilde{n}_k}{\partial t}\right|_{growth} - \frac{\tilde{n}_k}{\tau_{exchange}} \quad (9)$$

$$\frac{\partial n_i(r_i,t)}{\partial t} = \left.\frac{\partial n_i}{\partial t}\right|_{growth} + \left.\frac{\partial n_i}{\partial t}\right|_{coag} - \frac{n_i}{\tau_{sedim}} - \frac{n_i}{\tau_{exchange}} \quad (10)$$

where $\tilde{n}_k$ and n_i are molar concentrations of gas and aerosol species, respectively, and r_i is the aerosol particle size in bin i. P_k and L_k are chemical production and loss terms, while the time derivative terms describe changes due to particle growth and coagulation. $\tau_{exchange}$ and τ_{sedim} are timescales for exchange of material with the troposphere and adjacent stratospheric regions, and for aerosol sedimentation. The equations are solved using the Klopfenstein-Shampine algorithm (*ode15s* in Matlab).

The transformation of SO_2 into H_2SO_4 in the stratosphere proceeds by a chain of photochemical reactions, the most important of which are [*Turco et al.*, 1979a]

$$SO_2 + OH + M \rightarrow HSO_3 + M \quad (11)$$

$$HSO_3 + OH \rightarrow SO_3 + H_2O \quad (12)$$

$$SO_3 + H_2O \rightarrow H_2SO_4 \quad (13)$$

In our model, the chemical production and loss terms P_i and L_i are defined by the key sulfur reactions shown in Table S3. We neglect the outgassing of H_2S in our model. As we find that the SO_2 injection rates to the stratosphere required to force a Snowball transition are orders of magnitude lower than the upper limits on Franklin SO_2 outgassing rates, inclusion of H_2S would have added complexity to the model without fundamentally changing the nature of the conclusions.

The model is initialized by the injection of a given mass of SO_2 gas m_{SO_2} into the box. Injected masses are calculated as multiples of the SO_2 injected by Pinatubo [approx. $m_{SO_2,0}$ = 20 Mt; *Self et al.* [2014]]. The number density of H_2O and the background gas density [M] are calculated from a standard present-day atmospheric profile [*Anderson et al.*, 1986] (Table S2), while the OH number density is set to yield the characteristic SO_2 to H_2SO_4 conversion timescale observed after Pinatubo of 35 days [*Read et al.*, 1993]. The sensitivity of the results to changes in OH levels are described in the next section. At the first model timestep, the aerosol distribution is set to consist of condensation nuclei only. We assume that condensation nuclei are transported into the stratosphere along with the sulfur-bearing gas. The number concentration in the first particle bin is initialized as $n_1^0 = n_{Cn}(m_{SO_2}/m_{SO_2,0})$, where $m_{SO_2,0}$ = 20 Mt. We find that n_{Cn} = 100 particles cm^{-3} yields closest correspondence with Pinatubo observations. This value is similar to the observed condensation nuclei number density at the tropopause on present-day Earth [*Turco et al.*, 1979b]. Sensitivity of the results to variations in this parameter are also described in the next section.

Aerosol particle nucleation and growth

Aerosol particles grow through absorption of both H_2SO_4 and H_2O. Equilibration with H_2O is rapid, however, and the variation of equilibrium H_2O:H_2SO_4 droplet weight ratios with height in the atmosphere is not high [*Turco et al.*, 1979a]. For simplicity, here we assume that droplets have a fixed H_2SO_4 specific concentration $q_{H_2SO_4}$ = 0.75 kg/kg, a value appropriate to Earth's present-day lower stratosphere [*Turco et al.*, 1979a].

Aerosol particles are assumed to form on Aitken particles, which we treat as a monodisperse population of small ($r_p = 0.01$ μm) particles. The growth of particles by condensation of H_2SO_4 is given by

$$g = \frac{\mathrm{d}r_p}{\mathrm{d}t} = \frac{m_{\mathrm{H_2SO_4}} D_{\mathrm{H_2SO_4}} (\tilde{n}_{\mathrm{H_2SO_4}} - \tilde{n}_{sat,\mathrm{H_2SO_4}})}{r_p \rho_p q_{\mathrm{H_2SO_4}} (1 + \lambda_p \mathrm{Kn}_1)} \tag{14}$$

where r_p is the particle radius, ρ_d is the particle density, $m_{\mathrm{H_2SO_4}}$ is the molecular mass of H_2SO_4, $D_{\mathrm{H_2SO_4}}$ is the molecular diffusion coefficient of H_2SO_4 in air (calculated following the procedure for trace gases described in *Jacobson* [2005]), $n_{\mathrm{H_2SO_4}}$ is the number density of H_2SO_4 molecules near the droplet and $n_{sat,\mathrm{H_2SO_4}}$ is the H_2SO_4 condensation number density [*Turco et al.*, 1979a]. The latter is derived from the H_2SO_4 vapor pressure curve, for which we use the coefficients given in *Kulmala and Laaksonen* [1990]. Growth rate was then converted to the rate of change of aerosol number concentration by a derivative with respect to particle radius

$$\left.\frac{\partial n_i}{\partial t}\right|_{growth} = -\frac{\partial}{\partial r}\left(g n_i\right). \tag{15}$$

$\mathrm{Kn}_1 = l_{\mathrm{H_2SO_4}}/r_p$ is the Knusden number for H_2SO_4 diffusion in air, while we define λ_p here as

$$\lambda_p = \frac{1.33 + 0.71/\mathrm{Kn}_1}{1 + 1/\mathrm{Kn}_1}. \tag{16}$$

The H_2SO_4 diffusion coefficient $D_{\mathrm{H_2SO_4}}$ and mean free path in air $l_{\mathrm{H_2SO_4}}$ were calculated using standard methods [*Jacobson*, 2005], with Sutherland's formula

$$\eta_a = 1.8325 \times 10^{-5} \left(\frac{416.16}{T_{strat} + 120}\right) \left(\frac{T_{strat}}{296.15}\right)^{1.5} \tag{17}$$

used to calculate the dynamic viscosity of air as a function of temperature.

Aerosol particle sedimentation

Sedimentation is modeled using the Stokes velocity equation

$$v_{sedim} = \frac{2}{9} f_C r_p^2 g \rho_p / \eta_a, \tag{18}$$

where g is gravity and ρ_a is air density. Here

$$f_C = 1 + \mathrm{Kn}_2 (A + B e^{-C/\mathrm{Kn}_2}) \tag{19}$$

is the Stokes-Cunningham low pressure correction factor, with $A = 1.249$, $B = 0.42$, $C = 0.87$, $\mathrm{Kn}_2 = l_{air}/r_p$ the Knudsen number for air diffusion and l_{air} the mean free path of air [*Jacobson*, 2005]. The sedimentation timescale is then calculated as $\tau_{sedim} = z_{fall}/v_{sedim}$, where $z_{fall} = 5.9$ km is the distance that an average particle needs to fall to exit the stratosphere.

Aerosol particle coagulation

When they collide, aerosol particles may coagulate. Over time this process shifts the particle distribution towards larger radii, increasing the sedimentation rate and decreasing the radiative forcing per unit mass. We describe coagulation using the discrete equation

$$\left.\frac{\partial n_i}{\partial t}\right|_{coag} = +\frac{1}{2} \sum_{j=1}^{i-1} K_{j,i-j} n_j n_{i-j} - n_i \sum_{j=1} K_{i,j} n_j \tag{20}$$

where n_i is the aerosol number concentration in the ith bin, t is time and $K_{i,j}$ is the coagulation kernel. Total particle volume conservation is ensured by use of a bin-dependent volume fraction correction term [*Jacobson et al.*, 1994]. We validated our coagulation scheme by comparison with analytical results for the constant $K_{i,j} = K_0$ case [Smoluchowski's result; see e.g. *Seinfeld and Pandis* [2012]].

The coagulation kernel is calculated using the Fuchs equation, which is valid both in the high and low particle Knudsen number regimes. Specifically, for two particles of diameter

$d_{p,1}$ and $d_{p,2}$, we define

$$K_{12} = 2\pi(D_1 + D_2)(d_{p,1} + d_{p,2})\beta \tag{21}$$

with

$$\beta = \left[\frac{d_{p,1} + d_{p,2}}{d_{p,1} + d_{p,2} + 2\sqrt{g_1^2 + g_2^2}} + \frac{8(D_1 + D_2)}{\sqrt{(c_1^2 + c_2^2)}(d_{p,1} + d_{p,2})} \right]^{-1}, \tag{22}$$

$$g_i = \frac{1}{3d_{p,i}l_i} \left[(d_{p,i} + l_i)^3 - (d_{p,i}^2 + l_i^2)^{3/2} \right] - d_{p,i}, \tag{23}$$

mean particle speed

$$c_i = \sqrt{\frac{8k_B T}{\pi m_i}}, \tag{24}$$

mean free path

$$l_i = \frac{8D_i}{\pi c_i}, \tag{25}$$

and particle diffusivity

$$D_i = \frac{k_B T f_C}{3\pi\eta_a d_{p,i}} \tag{26}$$

with m_i the particle mass and k_B Boltzmann's constant [*Seinfeld and Pandis*, 2012]. Our coagulation physics is appropriate to the interaction of H_2SO_4 aerosol particles in the stratosphere that form from SO_2 days to weeks after an eruption [*Turco et al.*, 1979a, b; *Pinto et al.*, 1989]. More complex aggregation processes may occur for volcanic ash in plumes in the immediate aftermath of eruptions [*Telling and Dufek*, 2012; *Carazzo and Jellinek*, 2013], but for simplicity we do not consider the short-term climate effects of ash and dust here.

1.7. Bifurcation Plot

Figure 3B in the main text was produced using a classical Budkyo-Sellers type model of the ice-albedo feedback. We assume that surface albedo depends on temperature as

$$A(T) = \begin{cases} A_i & T \leq T_i \\ A_0 + (A_i - A_0)\frac{(T-T_0)^2}{(T_i-T_0)^2} & T_i < T < T_0 \\ A_0 & T \geq T_0 \end{cases} \quad (27)$$

with T_0 the temperature at which ice entirely disappears from the surface, T_i the temperature at which ice coverage is global, A_i the albedo of snow/ice and A_0 the albedo of the ice-free planet. Justification of the terms in this equation are given in e.g., *Pierrehumbert* [2011]. Here we take representative values $T_i = 260$ K, $T_0 = 290$ K and $A_i = 0.6$. A_0 is set to be 0.24, as in the ice-free tropopause height simulations. The radiative-convective model was then run assuming a 1 bar N_2 atmosphere and various CO_2 molar concentrations to produce absorbed solar radiation and outgoing longwave radiation for a range of surface temperatures T_s. The radiative imbalance $\Delta F = OLR - ASR$ was then produced as a function of T_s via interpolation.

In some coupled 3D general circulation models with ocean dynamics included, Neoproterozoic Snowball glaciations occur close to lower CO_2 partial pressures than those modeled here [*Voigt and Marotzke*, 2010; *Pierrehumbert et al.*, 2011; *Yang et al.*, 2012]. While we do not attempt to capture the effects of sea ice and ocean dynamics here, we note that the basic effects of aerosol forcing would play out similarly starting from a lower CO_2 climate state. As discussed in the main text, CO_2 levels, while not well constrained prior to glacial onset, were probably low due to the predominance of low-latitude continents [*Li et al.*, 2013] and enhanced global weatherability [*Marshall et al.*, 1988].

1.8. Ocean Thermal Inertia

The energy balance equation for the tropical ocean mixed layer can be approximated as

$$\frac{\mathrm{d}}{\mathrm{d}t}(\rho_w c_{p,w} T d) = ASR - OLR = \Delta F \tag{28}$$

with $\rho_w = 1000$ kg/m^3 the density of liquid water, $c_{p,w} = 4200$ J/kg/K the heat capacity of liquid water, T temperature and d the depth of the mixed layer [*Pierrehumbert*, 2011]. For a radiation imbalance ΔF caused by aerosol forcing we can write the characteristic cooling timescale as

$$\tau_{cool} = \frac{\rho_w c_{p,w} d \Delta T}{\Delta F} \tag{29}$$

Given $\Delta F = 10$ W/m^2, a required global mean ΔT of 5 K and a mixed layer depth of 50 m, $\tau_{cool} = 3.3$ y. This simple calculation neglects the enhanced vertical mixing that has been observed in some coupled ocean-atmosphere GCM simulations of Snowball transitions [*Voigt and Marotzke*, 2010], and hence may represent a lower limit on the required timescale.

2. Model Validation and Sensitivity Tests

2.1. Radiative-convective climate model

To validate our radiative-convective model, we ran it assuming present-day globally averaged insolation and surface pressure, clear-sky conditions and a solar zenith angle of 60°. Results are shown in Figure S2. As can be seen, the model reproduces Earth's present-day mean temperature profile reasonably accurately.

2.2. Volcanic plume model

We compared our plume model with analytic and numerical results from the literature [*Morton et al.*, 1956; *Stothers et al.*, 1986; *Glaze and Baloga*, 1996]. Figure S3 shows the results of a single simulation with moderate values of heat flux and initial plume velocity. This figure reproduces Fig. 2 in *Glaze and Baloga* [1996], validating our model. Figures S4-S5 show the results of the combined plume / tropopause height modelling for different atmospheric ozone and nitrogen abundances. These figures demonstrate that our conclusions are not dependent on uncertainties in these parameters.

2.3. Aerosol Microphysics

In addition to testing subcomponents of the model vs. analytic results (see previous section), we validated the aerosol microphysical model by comparison with observations of the Pinatubo eruption event. Given a single injection of 20 Mt SO_2 into the tropical stratosphere, our model predicts a global mean radiative forcing of -2.0 W/m^2 over two years, which falls in the -1 to -3 W/m^2 range observed in the two years after Pinatubo [*McCormick et al.*, 1995]. Our predicted peak optical depth at 0.5 μm wavelength is 0.2 and our peak effective particle radius is around 0.5 μm, both of which are also close to the observed post-Pinatubo values [*Russell et al.*, 1996]. Finally, our peak aerosol sulfur mass burden is 8 Mt of S, which is close to the values obtained by complex 3D models with coupled microphysics and chemistry (Figure S6) [*Dhomse et al.*, 2014]. To test the response of the microphysical model to uncertain parameters, we also performed a range of sensitivity studies. See Table S4 for details.

Figure S7 shows the effective particle radius (as defined in *Hansen and Travis* [1974]) and stratospheric aerosol S burden as a function of time for the three simulations displayed in Figure 3A in the main text. Figure S8 shows the radiative forcing from a similar set of simulations run in a domain centered on the mid-latitude northern hemisphere, assuming an ice-covered surface. Radiative forcing is significantly less negative in this case due to the increased surface albedo, which decreases the aerosol cooling effect. Aerosol transport rates from mid-latitudes to the tropics in the stratosphere are slow, so in contrast to the Franklin LIP, a high-latitude eruption would be unlikely to force a Snowball transition. Finally, we also tested the dependence of our radiative forcing predictions on the pre-aerosol planetary albedo. The results are shown in Fig. S9.

Age constraints on Sturtian glaciation, techniques and data sources

Location	Age (Ma)	(+)	(-)	Technique	Mineral/Grains	Formation	Rel.	Reference
NWT, Laurentia	711.3	0.3	0.3	U-Pb CA-ID-TIMS	detrital zircon	Sayeuni	syn	Baldwin et al., 2016
Oman, Arabia	711.5	0.3	0.3	U-Pb CA-ID-TIMS	magmatic zircon	Ghubrah	syn	Bowring et al., 2007
South China	714.0	8.0	8.0	U-Pb SIMS	magmatic zircon	Liantuo	max	Lan et al., 2015
South China	715.9	2.8	2.8	U-Pb SIMS	magmatic zircon	Gongdong	max	Lan et al., 2014
South China	716.1	3.4	3.4	U-Pb SIMS	magmatic zircon	Gongdong	max	Lan et al., 2014
Yukon, Laurentia	716.5	0.2	0.2	U-Pb CA-ID-TIMS	magmatic zircon	Eagle Creek	syn	Macdonald et al., 2010
Idaho, Laurentia	717.0	4.0	4.0	U-Pb SHRIMP	clast in diamictite	Pocatello	max	Fanning & Link, 2004
Yukon, Laurentia	717.4	0.1	0.1	U-Pb CA-ID-TIMS	magmatic zircon	Mt. Harper Vol.	max	Macdonald et al., 2010
Arctic Alaska	719.5	0.3	0.3	U-Pb CA-ID-TIMS	detrital zircon	Kikitak Vol.	max	Cox et al., 2015
Virginia, Laurentia	722.0	3.0	3.0	U-Pb ID-TIMS	bulk zircon	Robinson River Vol.	max	Tollo & Aleinikoff, 1996
South China	724.0	12.0	12.0	U-Pb SHRIMP	detrital zircon	Liantuo	max	Gao & Zhang, 2009
Virginia, Laurentia	724.0	3.0	3.0	U-Pb ID-TIMS	bulk zircon	Robinson River Vol.	max	Tollo & Aleinikoff, 1996
Tarim, China	725.0	10.0	10.0	U-Pb SHRIMP	magmatic zircon	Bayisi	max	Xu et al., 2009
South China	725.0	10.0	10.0	U-Pb SHRIMP	detrital zircon	Banxi	max	Zhang et al., 2008

Age constraints on Franklin large igneous province, techniques and data sources

Location	Age (Ma)	(+)	(-)	Technique	Mineral/Grains	Formation	Rel.	Reference
Devon Island	712	2	2	U-Pb ID-TIMS	bulk baddeleyite	Granville Fjord sill	sill	Denyszyn et al., 2009b
Ellesmere Island	713	2	2	U-Pb ID-TIMS	single grain baddeleyite	Clarence head	dike	Denyszyn et al., 2009a
Ellesmere Island	713	3	3	U-Pb ID-TIMS	bulk baddeleyite	Clarence head	dike	Denyszyn et al., 2009a
Victoria Island	714.2*	2.6	2.5	upper-intercept	bulk baddeleyite	Low. Sills, Shaler Gp	sill	Heaman et al., 1992
Ellesmere Island	716	1	1	U-Pb ID-TIMS	single grain baddeleyite	Clarence head	dike	Denyszyn et al., 2009a
Borden	716	4	5	U-Pb ID-TIMS	bulk baddeleyite	Borden dikes	dike	Pehrsson & Buchan, 1999
Victoria Island	716.3	0.5	0.5	U-Pb ID-TIMS	single grain baddeleyite	Sill 6a, Shaler Gp	sill	Macdonald et al., 2010
Bathhurst Inlet	720*	1	1	Pb-Pb ID-TIMS	bulk baddeleyite	Quadyuk Is. gabbro	sill	Heaman et al., 1992
Baffin Island	720*	4	4	Pb-Pb ID-TIMS	bulk baddeleyite	Cumberland dike	dike	Heaman et al., 1992
Coronation Gulf	720*	6	6	Pb-Pb ID-TIMS	bulk baddeleyite	Rae Group	sill	Heaman et al., 1992
Borden	720	8	8	U-Pb ID-TIMS	bulk baddeleyite	Borden dikes	dike	Pehrsson & Buchan, 1999
Greenland	721	4	4	U-Pb ID-TIMS	1 & 2 grain baddeleyite b.f.	Qaanaaq dike	dike	Denyszyn et al., 2009b
Ellesmere Island	721	2	2	U-Pb ID-TIMS	1 & 2 grain baddeleyite b.f.	Cadogan Glacier dike	dike	Denyszyn et al., 2009b
Victoria Island	721*	5	2	upper-intercept	bulk baddeleyite	Up. Sills, Shaler Gp	sill	Heaman et al., 1992
Greenland	726*	24	24	upper-intercept	bulk baddeleyite	Belcher Glacier dike	dike	Denyszyn et al., 2009b

**Pb-Pb and upper intercept ages recalculated from isotope ratios using the U decay constant ratio of Schoene et al. (2006).*
b.f. = bulk fraction

Table S1. Geochronological constraints on the onset of the Sturtian glaciation and the Franklin Large Igneous Province [*Baldwin et al.*, 2016; *Bowring et al.*, 2007; *Lan et al.*, 2014b, 2015; *Macdonald et al.*, 2010; *Fanning and Link*, 2004; *Cox et al.*, 2015; *Tollo and Aleinikoff*, 1996; *Xu et al.*, 2009; *Zhang et al.*, 2008; *Denyszyn et al.*, 2009a, b; *Heaman et al.*, 1992; *Pehrsson and Buchan*, 1999; *Schoene et al.*, 2006].

Table S2. Standard parameters used in the volcanic plume, climate and aerosol microphysics modeling.

Parameter	Values
Plume entrainment coefficient α	0.1
Specific heat capacity of atmosphere at constant pressure $c_{p,a}$	1040 J/K/kg
Specific heat capacity of volatiles in plume $c_{p,v}$	1900 J/K/kg
Specific concentration of fines in eruption q_f	0.01 kg/kg
Specific concentration of volatiles in eruption q_v	0.02 kg/kg
Magma density ρ_{magma}	2900 kg/m^3
Magma specific heat capacity c_{magma}	1100 J/K/kg
Solar flux F_V	1284 W m^{-2}
Surface pressure p_s	1.0 bar
Ice-free global mean surface albedo A_0	0.24
Ice-covered global mean surface albedo A_i	0.6
Total ice loss temperature T_0	290 K
Global ice coverage temperature T_i	260 K
Aerosol droplet H_2SO_4 specific concentration $q_{H_2SO_4}$	0.75 kg/kg
Sulfuric acid density $\rho_{H_2SO_4}$	1840 kg/m^3
Water density ρ_{H_2O}	1000 kg/m^3
H_2SO_4-air collision diameter $d_{H_2SO_4}$	4.3×10^{-10} m
Plume condensation nuclei parameter n_{Cn}	100 particles cm^{-3}
Troposphere-stratosphere exchange timescale $\tau_{exchange}$	1.0 y
Mean stratosphere temperature T_{strat}	218.6 K
Mean stratosphere pressure p_{strat}	5.3×10^3 Pa
Mean stratosphere OH concentration $\tilde{n}_{OH}$	5.5×10^5 molecules/cm^3
Mean stratosphere H_2O concentration $\tilde{n}_{H_2O}$	7.0×10^{12} molecules/cm^3

Table S3. Chemical reaction rates used in the aerosol microphysical model. When used, M is assumed to be background air. The rate coefficient of reaction (1) was checked against the more general formula given in *Sander et al.* [2006] and found to agree closely under the stratospheric conditions studied. The rate coefficient of reaction (4) was calculated by integrating loss rate values given in *Turco et al.* [1979b] over the altitude range of the box model.

#	Reaction	Rate coefficient	Reference
1	$SO_2 + OH + M \rightarrow HSO_3 + M$	$8.2 \times 10^{-13}/(7.0 \times 10^{17} + [M])$ cm^6 s^{-1}	*Turco et al.* [1979b]
2	$HSO_3 + OH \rightarrow SO_3 + H_2O$	1×10^{-11} cm^3 s^{-1}	*Turco et al.* [1979b]
3	$SO_3 + H_2O + H_2O \rightarrow H_2SO_4 + H_2O$	1.2×10^{-15} cm^3 s^{-1}	*Sander et al.* [2006]
4	$H_2SO_4 + h\nu \rightarrow SO_2 +$ products	3.8×10^{-12} s^{-1}	*Turco et al.* [1979b]

Table S4. Results from the aerosol microphysical model when key parameters are varied. $\langle M_{\mathrm{S}} \rangle$ and $\langle r_{eff} \rangle$ are the time-mean total S aerosol burden and particle radius, respectively. All simulations are run for three years with yearly eruptions that inject 100 Mt of SO_2 (5× Pinatubo).

Simulation	$\langle M_{\mathrm{S}} \rangle$ (Mt)	$\langle r_{eff} \rangle$ (μm)
Standard case, 5× Pinatubo	27.3	0.67
$\tilde{n}_{\mathrm{OH}} = 5.5 \times 10^4$ molecules/cm^3	11.2	0.68
$\tilde{n}_{\mathrm{OH}} = 5.5 \times 10^6$ molecules/cm^3	31.0	0.63
$n_{Cn} = 10$ particles cm^{-3}	24.3	0.83
$n_{Cn} = 1000$ particles cm^{-3}	28.3	0.63
$\tau_{exchange} = 0.5$ y	17.1	0.57
$\tau_{exchange} = 2$ y	35.8	0.75

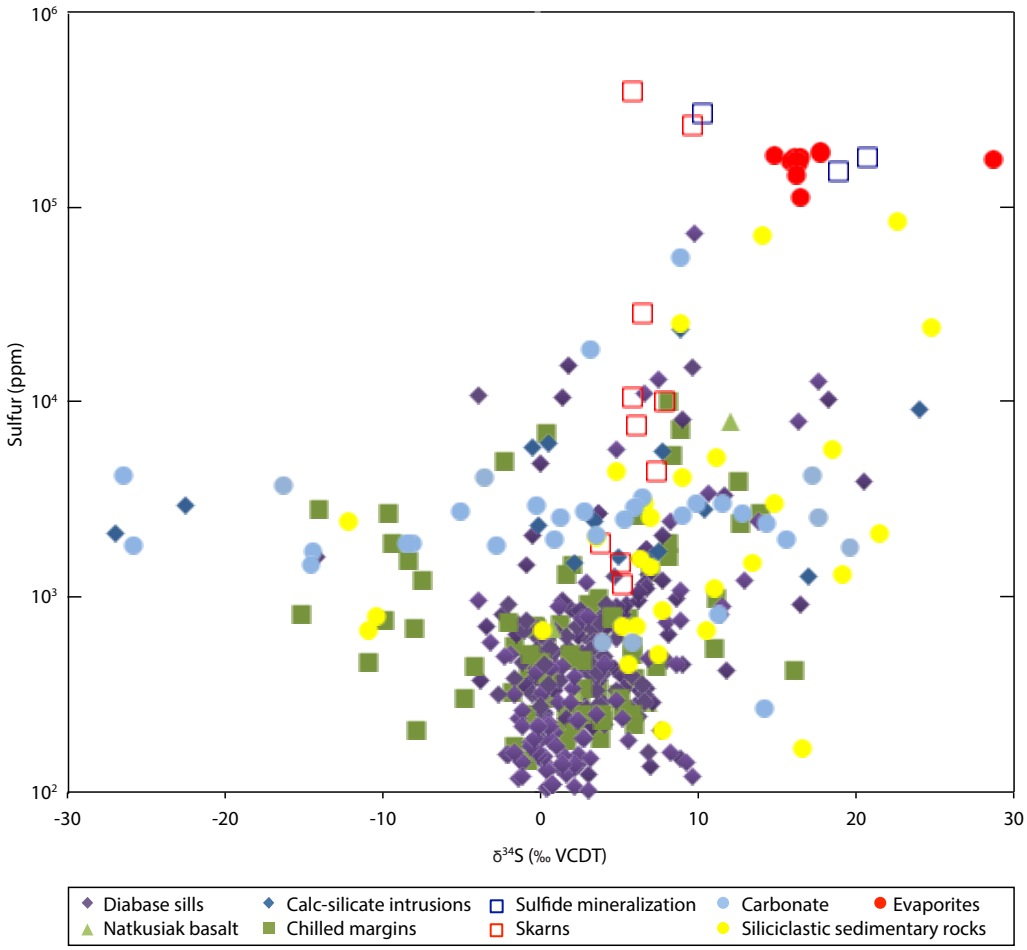

Figure S1. Sulfur concentration and isotope data from the Natkusiak magmatic assemblage, sedimentary rocks of the Shaler Supergroup, and contact metamorphic rocks. Data plotted from geochemical database of Franklin sills, Natkusiak Basalts and Shaler Supergroup rocks [*Bedard et al.*, 2016].

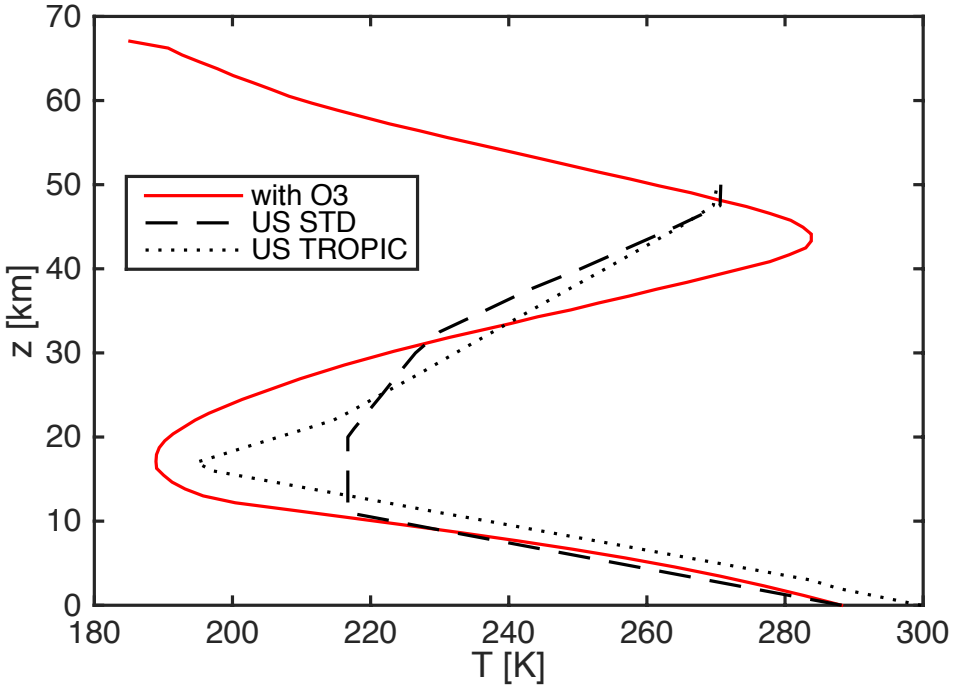

Figure S2. Radiative-convective equilibrium temperature profile for Earth's atmosphere under cloud-free conditions with CO_2 molar concentration of 300 ppmv, solar zenith angle of 60°, 1 bar atmospheric pressure and present-day insolation. The red line shows model results with ozone UV absorption included. Dashed and dotted lines show the US standard mid-latitude and tropical atmosphere, respectively.

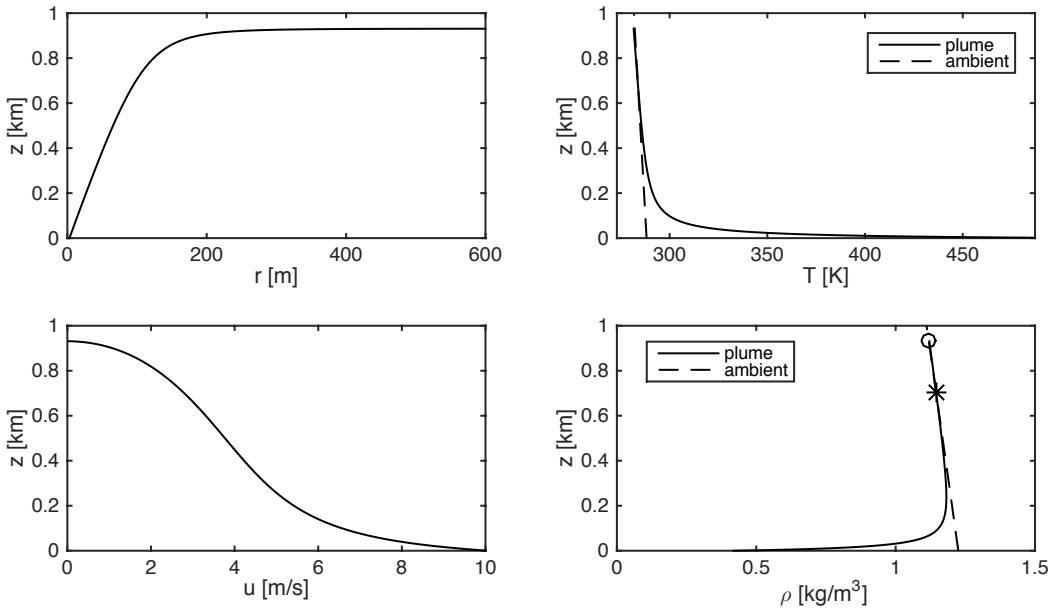

Figure S3. (top left) Plume radius (top right) temperature (bottom left) plume vertical speed and (bottom right) density vs. altitude as simulated by the axisymmetric plume model. In the bottom right panel, the circle and asterisk indicate the maximum plume height and the neutral buoyancy height, respectively. For this simulation we assumed $Q_0 = 5.6 \times 10^7$ J/s, $r_0 = 3$ m, $T_{g,0} = 525$ K and $u_0 = 10$ m/s and the same thermodynamic parameters as *Glaze and Baloga* [1996].

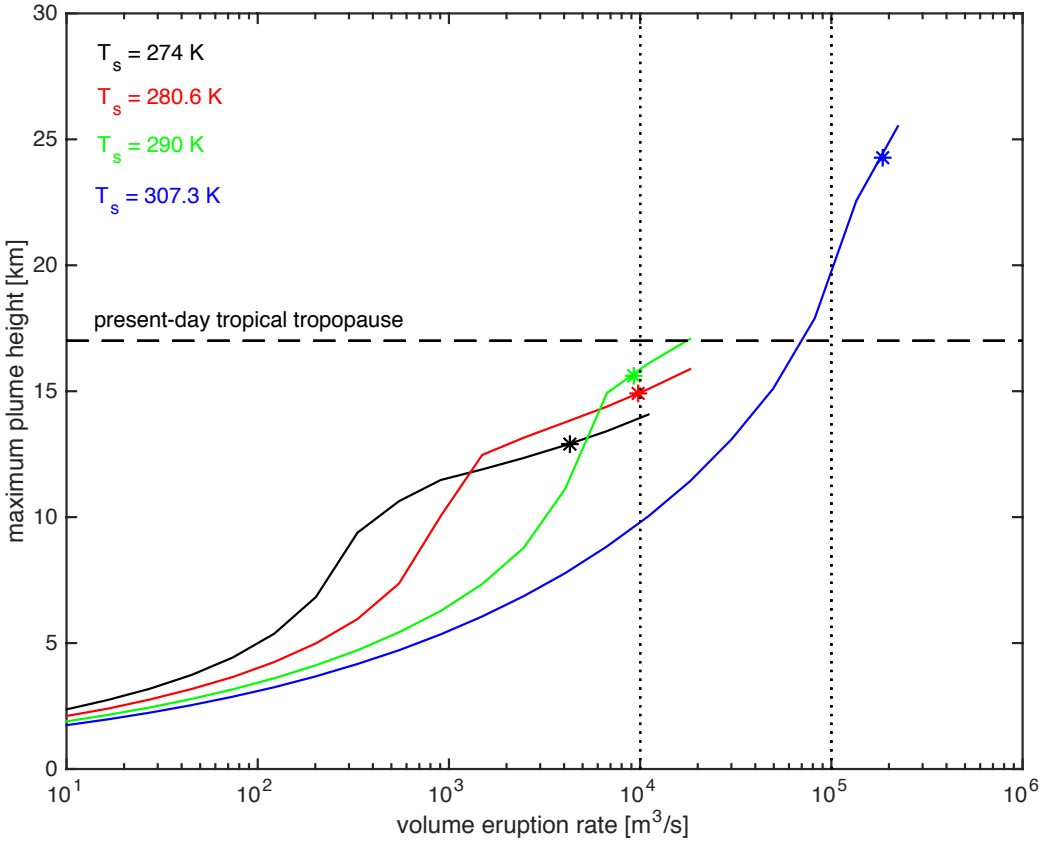

Figure S4. Same as Fig. 2B in the main text but assuming 10% of present-day ozone abundance.

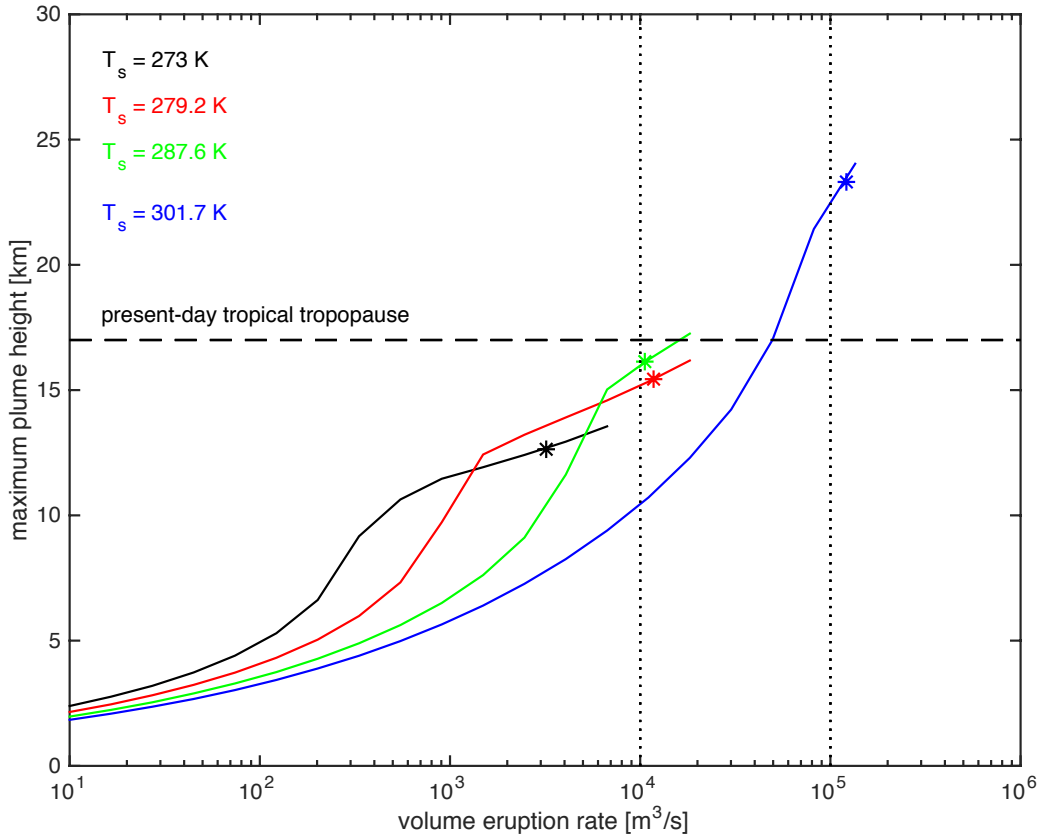

Figure S5. Same as Figure S4 but also assuming background N_2 pressure of 0.8 bar.

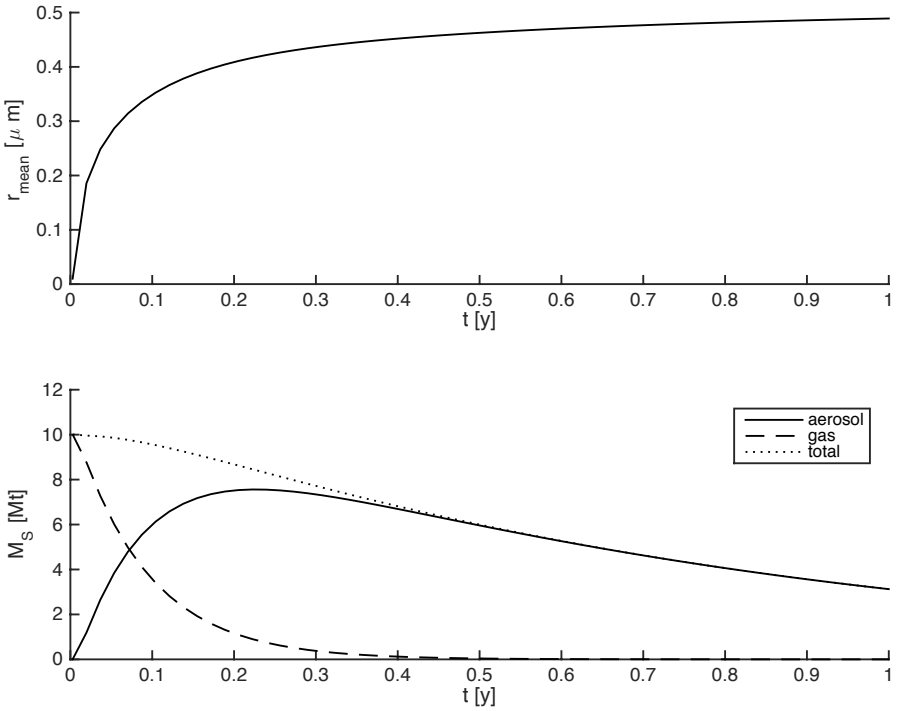

Figure S6. (top) Aerosol effective radius and (bottom) stratospheric sulfur loading as a function of time simulated by the aerosol microphysics model. The model initial conditions correspond to a single Pinatubo-like injection of 20 Mt SO_2 into the stratosphere.

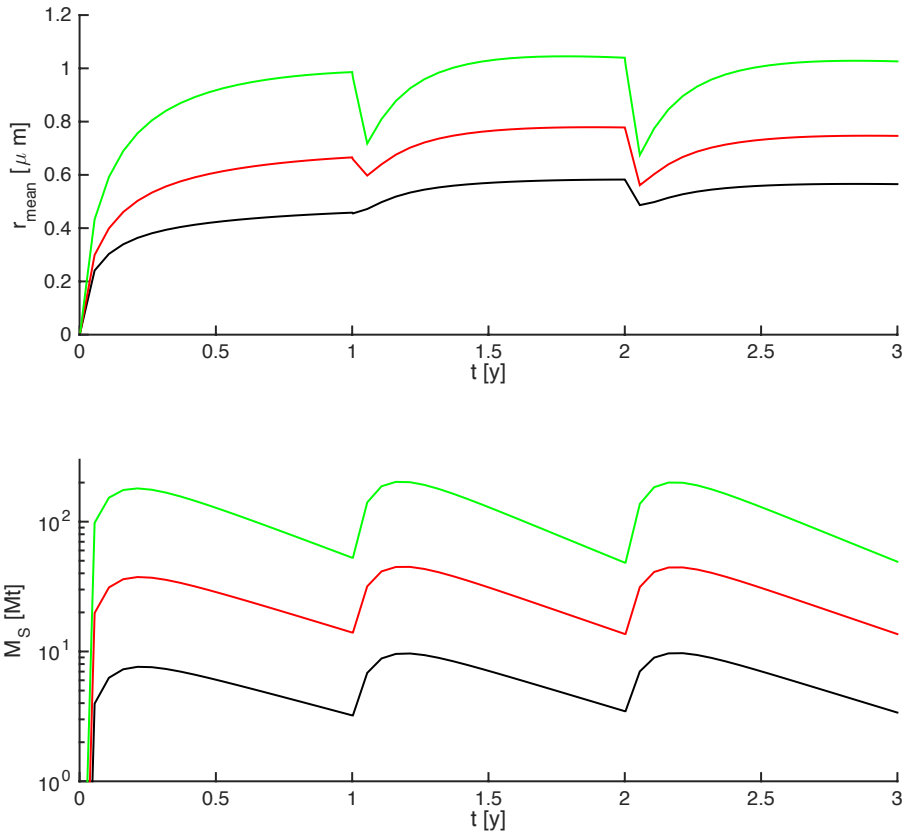

Figure S7. (top) Aerosol effective radius and (bottom) stratospheric aerosol S burden vs. time for the standard set of 1×, 5× and 25× Pinatubo aerosol forcing simulations (corresponds to Fig. 3A in the main text).

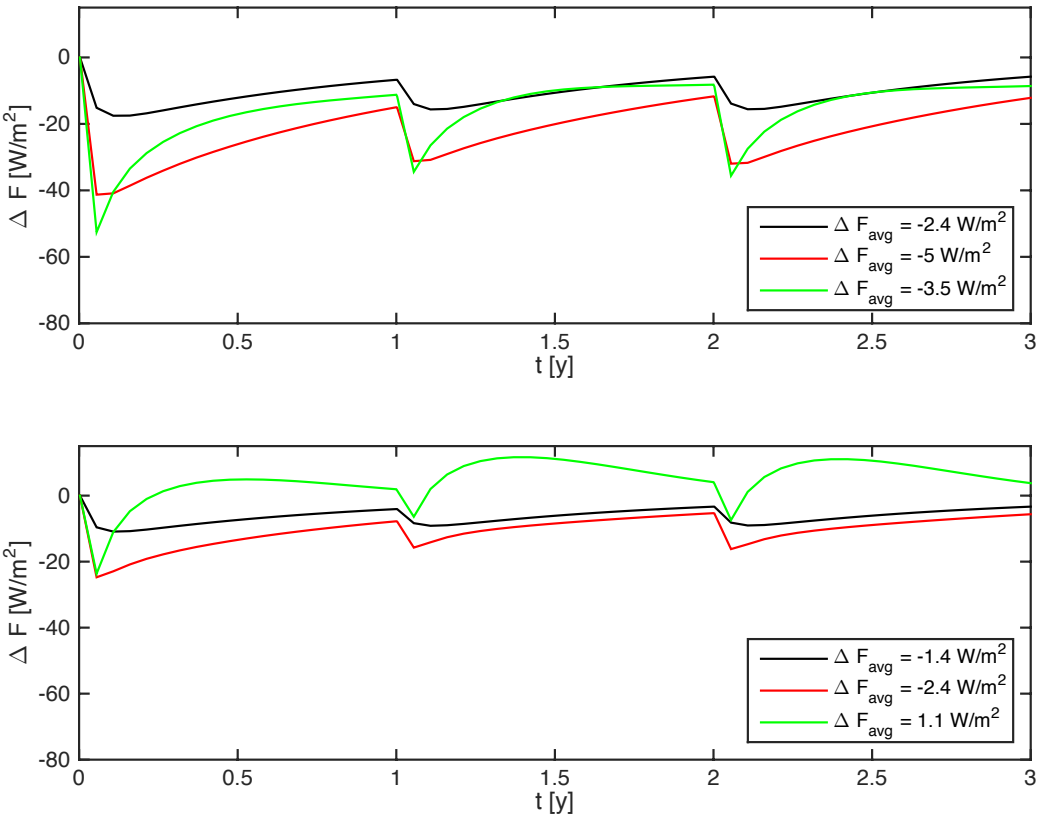

Figure S8. Same as Fig. 3A in the main text, except assuming a tropopause height of 10 km and simulation box domain from 30° N to 80° N, corresponding to the situation following a high latitude basaltic fissure eruption. The pre-aerosol mid-latitude planetary albedo is 0.365 (present-day value) in the top plot and 0.5 (high ice/snow cover case) in the bottom plot. At the highest eruption rate in the bottom plot, the combination of large aerosol particles and high pre-aerosol albedo leads to a small net warming.

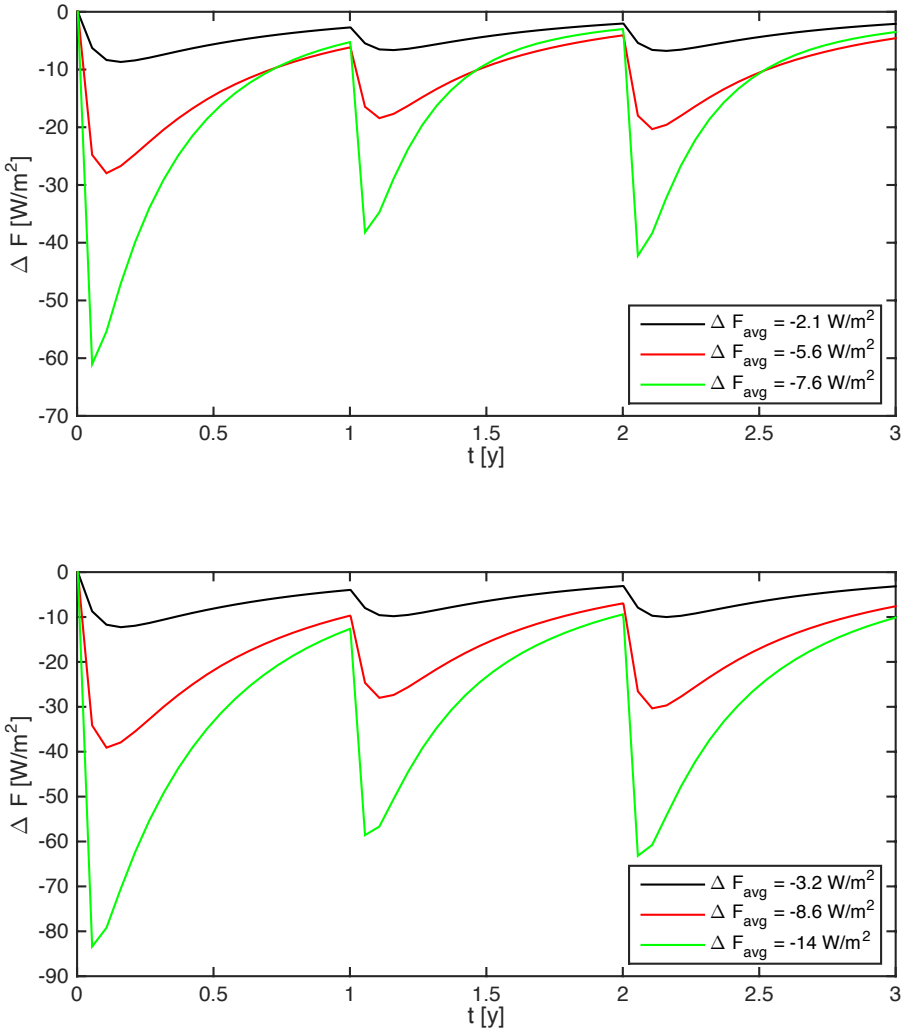

Figure S9. Same as Fig. 3A in the main text, except for pre-aerosol tropical planetary albedo of 0.3 (top plot) and 0.2 (bottom plot). The lines in the plot correspond to tropical mean radiative forcing, while the values in the legend are global means.